A GOLD@GRAPHENE OXIDE BIOSENSOR BASED ON PLASMON-ENHANCED FLUORESCENT AND FRET FOR INTRACELLULAR DETECTION OF MICRORNA IN DIFFERENTIATING T CELLS

LAM CHING YING

MPhil

The Hong Kong Polytechnic University

This programme is jointly offered by The Hong Kong Polytechnic University

2024

The Hong Kong Polytechnic University
Department of Biomedical Engineering

A GOLD@GRAPHENE OXIDE BIOSENSOR BASED ON PLASMON-ENHANCED FLUORESCENT AND FRET FOR INTRACELLULAR DETECTION OF MICRORNA IN DIFFERENTIATING T CELLS

Lam Ching Ying

A thesis submitted in partial fulfilment of the requirements for the degree of Master of Philosophy

September 2023

CERTIFICATE OF ORIGINALITY

I hereby declare that this thesis is my own work and that, to the best of my knowledge and belief, it reproduces no material previously published or written, nor material that has been accepted for the award of any other degree or diploma, except where due acknowledgement has been made in the text.

_____ (Signed)

_____Lam Ching Ying_____ (Name of student)

Abstract

Microribonucleic acid (miRNA) is a class of small single-strand RNA which controls cellular processes such as differentiation and apoptosis by undergoing gene silencing. Recent studies provoke a new insight that miRNA is likely playing, suggesting that miRNA is likely a crucial regulator in T cell subtype differentiation. Numerous miRNA profiling studies showed the expression level of miRNA changes during different differentiated states of CD8+ T-cells. MiRNAs such asmiR-21 and miR-150 dominantly expressed and exhibited profound changes in gene expression between naïve, effector, and memory $CD8^+$ T-cells. However, limited studies have attempted to trace T-cell differentiation from a miRNA perspective, which may provide novel insights into miRNA functions and potential therapeutic applications for future fundamental studies relating to T-cell immunotherapy. This study successfully developed a metal-enhanced fluorescence (MEF) nucleic acid-based nanoprobe to explore T-cell subtypes by sensing miRNA-150 and miRNA-21 on day 0, 1, 3, 5 and 7. The optimal MEF distance was approximately 18 nm with an enhancement factor of 2.8 times for FITC and 1.8 times for RITC. Notably, we further fortified these nanoparticles with a secondary silica coating layer, enhancing stability greatly for 21 days. These nanoprobes displayed a linear response to varying target DNA concentrations, boasting limits of detection (LoD) at a remarkable 28.859 pM for FITC-coated $AuSiO_2$ and 38.43 pM for RITC-coated $AuSiO_2$.

Acknowledgement

First of all, I would like to express my sincerest gratitude to my supervisor, Dr. Dexter Siu-hong WONG, for his unwavering support and invaluable guidance throughout my research journey. Dr. Dexter Wong's dedication to his students goes beyond academic guidance; he genuinely cares about our development as researchers and individuals. His constructive feedback, patience, and encouragement have been a constant source of motivation for me. I have learned the technical aspects of research and the importance of perseverance and resilience, qualities I will carry with me throughout my career. His influence will continue to shape my future endeavours. I look forward to applying the knowledge and skills I have gained under his tutelage as I pursue a successful research career.

Then, I would like to thank my co-supervisor, Professor Mo YANG, who inspired me to further my studies after my bachelor's degree and financially supported my project and research journey. I am profoundly grateful for the opportunities he has provided and his impact on my educational and research pursuits. I would also like to thank all of our group members, Dr Willis Ho, Dr. Ruolin Zhang, Dr. Qin Zhang, Dr. Bohan Yin, Yutian Gu, Yingying Huang, and YAN Jiaxiang for the assistance with lab work and constructive comments during my two-year Mphil study.

I want to thank Lejian Liu, my friend and colleague, for being so supportive during the happy and dark times, and thanks for the days we discussed our work and had lunch together. Last but not least, I would like to dedicate my gratitude to my parents and partner for their everlasting love and their encouragement for me to further my postgraduate studies.

Table of Contents

List of Abbreviations

APTEs	3-(aminopropyl)triethoxysilane
AuNPs	gold nanoparticles
$AuSiO_2$	gold-silica core-shell particles
DI water	deionised water
DNA	deoxyribonucleic acid
DLS	dynamic light scattering
DMF	N, N-Dimethylformamide
FITC	fluorescein isothiocyanate
FRET	fluorescence resonance energy transfer
GO	graphene oxide
$HAuCl_4$	gold(III) chloride trihydrate
LSPR	localised surface plasmon resonance
$MgCl_2$	magnesium chloride
miRNA	microRNA
NaCl	sodium chloride
RPMI 1640	Roswell Park Memorial Institute 1640 medium
qRT-PCR	quantitative reverse transcription polymerase chain reaction
RITC	rhodamine B isothiocyanate
RNA	ribonucleic acid
SMCC	succinimidyl-4-(N-maleimidomethyl)cyclohexane-1-carboxylate
TCEP	tris(2-carboxyethyl)phosphine hydrochloride
TEM	transmission electron microscopy
TEOS	tetraethyl orthosilicate
Thiol DNA	thiolated deoxyribonucleic acid
Thiol PEG	thiolated polyethylene glycol
UPW	UltraPure DNase/RNase-free distilled water

List of Figure

Chapter 1 Introduction

1.1 Background of T cells

The adaptive and innate immune systems are potent defences against infections and diseases. Immature T cells, namely, $CD4^+$ and $CD8^+$ T cell, originate in bone marrow, migrates to the thymus for maturation and develop specific T cell receptors on the cell surface[1]. Cytotoxic $CD8^+$ T cell modulates apoptosis of abnormal or infected cells while helper $CD4^+$ T cell maintains cytotoxic $CD8^+$ T cell response and prevents exhaustion[2]. Importantly, cytotoxic $CD8^+$ T cells play an essential role in adoptive immunotherapy, which dominates the anticancer immune response. Cytotoxic $CD8^+$ T cell is initially at a naïve state in the lymph node. It can be activated through peptide major histocompatibility complex (pMHC) class I binding with specific antigens from antigen-presenting cells (APCs)[3]. For example, a dendritic cell that displays a foreign antigen bound by pMHC class I on its surface after infection would be recognised by naïve cytotoxic $CD8^+$ T cells and activated cytotoxic $CD8^+$ T cell differentiation. After activation, naïve $CD8^+$ T cell differentiates into different central memory and effector T cell subsets. Effector $CD8^+$ T cell secrets cytokines and cytotoxic proteins, such as perforin, granzyme and granulysin, to activate macrophages and to program cell death for infected cells while central memory $CD8^+$ T cell is persistent and proliferative, which provides a long-term protective response against reinfection with the same pathogen. Therefore, cytotoxic $CD8^+$ T cells are essential for cancer eradication in the adaptive immune system [4].

1.2 Biogenesis of miRNA and its role in T cell

The cytotoxic $CD8^+$ T cells are highly involved in the adaptive immune system, while miRNA is known to regulate T cell development, maturation, differentiation and functions[5]. miRNA is a class of short and single-strand non-coding RNA with around 18 to 25 nucleotides, which is vital in gene silencing and regulating physiological and cellular processes such as cell proliferation, differentiation, apoptosis, and drug resistance[6]. miRNA is transcribed from DNA in the nucleus by RNA polymerase II before forming a hairpin structure primary miRNA. Nucleic DROSHA and DGCR8 protein recognise the primary miRNA to generate precursor miRNA, which is exported to the cytoplasm by exportin 5 and cleaved by a complex composed of DICER into double-strand miRNA. The miRNA duplex incorporates an Argonaute protein 2 (AGO2) forming RNA-induced silencing complex (RISC), which would unwound duplex miRNA forming two single-strand miRNAs, namely, a guide miRNA and a passenger miRNA.

The latter undergoes degradation quickly while the former incorporates into the RISC complex, and the guide miRNA is partially complementary to the 3'untranslated region (3'-UTR) of messenger ribonucleic acid (mRNA) to either inhibit mRNA translation or initiate mRNA degradation[7-9]. The non-perfect complementary hybridising characteristic of guide miRNA and mRNA contributes to the fact that a single miRNA can regulate different target mRNA; thus, the role of a miRNA varies significantly among different cell types and modulates the development and differentiation of cells[6]. Due to miRNA target complexity, mapping the binding sites of miRNA to target mRNA and correlating to the function of miRNA remain unclear.

A study conducted by Trifari and his colleagues suggested that T cell differentiation was subjected to the changes in the gene expression level of miRNA by deletion of depletion of DICER in human-activated cytotoxic $CD8^+$ T cells [10]. The deficiency of DICER caused upregulation of perforin, granzymes and effectors cytokines, leading to dysregulation of activation and proliferation of cytotoxic $CD8^+$ T cells[10]. Therefore, it is highly postulated that dysregulation of miRNA levels alters the translation of multiple protein-coding genes during cell differentiation [11]. Moreover, numerous miRNA profiling studies demonstrated significant changes in the gene expression level of miRNA during different cytotoxic CD8+ T cell states, postulating that miRNA played a vital role in regulating $CD8^+$ T cell differentiation and controlling its survival and function [12, 13]. Thus, such significant changes in gene expression might characterise different subsets of cytotoxic $CD8^+$ T cells. For instance, a few miRNAs dominantly expressed and exhibited profound changes in gene expression between naïve, effector, and memory cytotoxic $CD8^+$ T cells such as miRNA-21and miRNA-150 confirmed by three different approaches which were RNA cloning, miRNA microarray analysis and real-time PCR [12]. Expression of these seven miRNAs accounted for around 60% of all miRNAs, suggesting these miRNAs may control the key transcription factors to cytotoxic $CD8^+$ T cell differentiation[12]. Most miRNAs, including miRNA-150, downregulated in effector $CD8^+$ T cells compared to naïve $CD8^+$ T cells and upregulated in memory T cells compared to the effector $CD8^+$ T cell. Conversely, a few miRNAs, such as miRNA-21, showed an upregulation in effector $CD8^+$ T cells and a downregulation in memory $CD8^+$ T cells[7, 12]. The dynamic changes in the expression level of miRNA-150 and miRNA-21 are listed in Table 1. The unique concentration difference of miRNA-21 and miRNA-150 in different subsets of $CD8^+$ T cells may serve as novel indicators to monitor $CD8^+$ T cell differentiation. The aforementioned

systematic miRNA knock-out and profiling studies demonstrated miRNAs were certainly involved and behaved differently in T cell differentiation, cell survival, and apoptosis. However, limited studies have attempted to monitor T-cell differentiation from a miRNA perspective, which may provide a novel insight into adoptive immunotherapy by understanding and identifying the plasticity of $CD8^+$ T cells.

Table 1. Differential expression of miRNA-150 and miRNA-21 in T-cell subsets[12]

miRNA	Naïve T cell	Effector T cell	Memory T cell
miRNA-21	+	+++	++
miRNA-150	+++	+	++

1.3 Impact of miRNA-150 and miRNA-21 during T cell differentiation

To date, a range of microRNAs (miRNAs) have been acknowledged as central contributors in orchestrating immune responses, with miRNA-150 standing out as a noteworthy participants. miRNA-150 holds prominence for its abundant expression in naïve T cells [12, 14]. It has also been identified with multiple targets, including Foxo1, TCF1, c-Myb, and CD25, indicating its pivotal role in CD8 T cell biology [4, 15, 16]. Ban et al. suggested that miR-150 suppressed the expression of two critical factors, forkhead box O1 (Foxo1) and T cell-specific transcription factor 1 (TCF1) [4]. These factors also played a role in promoting the development of memory $CD8^+$ T cells, underscoring the significant role of miRNA-150 as a regulator in memory T cell differentiation[4]. Their study observed that miRNA-150 knockout mice predominantly differentiated into memory cells, exhibiting enhanced production of effector cytokines. Additionally, miRNA-150-deficient memory $CD8^+$ T cells displayed an augmented recall response and improved defence against infections caused by various viruses and bacteria. Moreover, Chen et al. demonstrated that miR-150 suppresses memory CD8 T cell development through c-Myb, a transcription factor [15]. Their research revealed that overexpression of miRNA-150 led to an upregulation of c-Myb, consequently decreasing the central memory T cell population. Conversely, subsequent experiments showed that reduced expression of miRNA-150 at later time points led to an increase in central memory T cells. Furthermore, Zhang et al. found that miR-150 suppresses the presence of the IL-2 receptor alpha chain

(known as IL-2Ra or CD25) in $CD8^+$ T cells [17]. The deficiency of miRNA-150 in T cells demonstrates increased levels of IL-2Ra, leading to heightened proliferation and a quicker progression towards differentiation. It is plausible that miRNA-150 plays a pivotal role in the viability of effector $CD8^+$ T cells, facilitating their transformation into memory cells through the modulation of IL-2 signalling. Thus, miRNA-150 emerges as a critical player in differentiating and maintaining central memory T cells. This makes it a potential and representative miRNA in T cell differentiation, particularly in guiding T cells towards a memory cell fate.

The majority of miRNAs are immediately down-regulated after T cell activation. However, miRNA-21 are the exception, showing an inverse pattern characterised by up-regulation in effector T cells but progressively decline in central memory T cells [12, 17-19]. Hence, it can be anticipated that these miRNAs promote the differentiation of terminal effector cells. Among these, miRNA-21 holds prominence for its abundant expression in naïve T cells [12]. Liang suggested that miRNA-21 cooperate with miRNA-155 to promote CD8 T+ cell activation by repressing SOCS1 and DUSP10 [20]. Two studies conducted in mice have substantiated the significance of miR-21 in autoimmune T-cell responses. When miRNA-21 is overexpressed in T cells, it leads to the development of autoimmune cholangitis in vivo. Conversely, inhibiting miRNA-21 in T cells reverses key indicators of autoimmunity in mice prone to lupus [21, 22]. These effects are attributed to the capability of miRNA-21 to suppress PDCD4, a specific protein translation inhibitor of genes crucial for the survival and function of effector T cells [23, 24]. Moreover, Kim et al. found that upregulation of miRNA-21 promotes effector T-cell differentiation [25]. Notably, the upregulation of miRNA-21 was associated with the induction of inflammatory and cytotoxic genes, including IL2RA, GZMB, CCL3, and CCL4 [25]. Conversely, reducing miRNA-21 expression during activation promoted the transcription of genes associated with forming memory T cells, including IL7R, BTLA, CD44, and CXCR3 [26]. Reducing the elevation in miRNA-21 expression resulted in the induction of a gene expression pattern characteristic of murine memory CD8+ T cells [27].

MiRNA-150 and miRNA-21 were chosen for intracellular miRNA detection during T-cell differentiation due to their crucial roles in immune responses. Both miRNA-150 and miRNA-21 are the abundant miRNA in CD8+ T cells. They distinctly impact gene expression, affecting

effector and memory T cell differentiation. The decrease in miRNA-150 expression level favour central memory T cell while the increase in miRNA-21 favour effector T cell. These dynamic expression patterns hold potential as novel indicators for monitoring CD8+ T cell differentiation.

1.4 Current Method and Research Gap

The traditional method to characterise the $CD8^+$ T cell subset by quantifying the expression level of surface biomarkers such as CD24 and CD62L of the $CD8^+$ T cell [28], which was time-consuming and required expensive and sophisticated instrument, while traditional miRNA detection relied on northern blotting, microarray analysis and reverse transcription polymerase chain reaction (RT-PCR)[29]. Northern blotting was the standard approach to detect miRNA but was time-consuming and required a large amount of RNA sample[30]. Microarray analysis had multiplexity and high performance but poor sensitivity[31]. RT-PCR was highly sensitive and specific, but it was the complexity and high demand for skilful labour[32]. These traditional methods for nucleic acid detection were primarily designed for extracellular settings and were not well-suited for intracellular applications. In contrast, intracellular nucleic acid detection requires specialised approaches and probes that can effectively navigate the complexities of the cellular environment. Nanomaterials have attracted significant attention recently due to their minute scale, substantial surface area-to-mass ratio, heightened reactivity, and applicability in intracellular detection[33-35]. Notably, graphene-based nanomaterials and AuNPs have emerged as promising candidates for intracellular nucleic acid detection.

The utilisation of graphene oxide (GO) offers several distinctive advantages in this context. Firstly, GO's substantial surface area provides ample binding sites for DNA or RNA probes, facilitating the efficient immobilisation of recognition elements and thereby enhancing sensitivity[36, 37]. Additionally, its recognised biocompatibility and low cytotoxicity ensure suitability for intracellular applications without compromising cellular viability[38, 39]. This, coupled with facilitated cellular uptake, allows for the effective delivery of sensing probes into the intracellular environment[40, 41]. Furthermore, GO exhibits robust fluorescence quenching properties, making it an effective platform for fluorescence-based intracellular sensing, enabling real-time monitoring of nucleic acid dynamics[42, 43]. Its layered structure allows for straightforward functionalisation with DNA probes or other recognition elements, enabling the

design of tailored assays for specific nucleic acid sequences[33, 37, 38]. The stability of GO in diverse environmental conditions ensures the reliability and reproducibility of detection assays within the intracellular milieu[35, 44]. By deploying various functionalised GO probes, it becomes possible to simultaneously detect multiple DNA targets within the same cell, enabling multiplexed intracellular nucleic acid sensing[45]. Thus, the distinctive properties of graphene oxide position it as a pivotal tool for intracellular nucleic acid detection.

Similarly, utilising AuNPs in nucleic acid detection and intracellular sensing presents several notable advantages. Their inherent stability ensures the reliability and reproducibility of detection assays, regardless of whether they are employed in solution or immobilised on various substrates[46]. The expansive surface area-to-volume ratio of AuNPs facilitates efficient functionalisation with biomolecules, such as DNA probes or antibodies, permitting the attachment of a diverse array of recognition elements, thereby enhancing sensitivity[33]. Moreover, the biocompatibility and low cytotoxicity of AuNPs render them suitable for intracellular sensing applications without compromising cellular viability[47, 48]. The unique optical feature, referred to as Localized Surface Plasmon Resonance (LSPR), can be intentionally tailored to enhance signal amplification, offering a significant advantage in detecting low-abundance nucleic acid targets[49-52]. The facile functionalisation of AuNPs further allows for the design of tailored assays customised to specific nucleic acid sequences or cellular targets[53, 54]. Overall, the utilisation of both graphene oxide and gold nanoparticles demonstrates their pivotal roles in advancing the capabilities of intracellular nucleic acid detection.

In contemporary research, there is a significant focus on the development of intracellular biosensing platforms that offer high sensitivity, cost-effectiveness, and simplicity in preparation. Given the challenge of low detection limits within cells, AuNPs nucleic acid-based detection is frequently integrated with nucleic acid amplification techniques to enhance sensitivity. However, enzyme-assisted nucleic acid amplification methods like PCR, loop-mediated isothermal amplification (LAMP), and CRISPR-Cas12 entail the use of numerous primers and enzymes[55-58]. This poses a higher risk of contamination and requires costly reagents. In contrast, metal-enhanced fluorescence (MEF) sensing offers an alternative approach. It relies on the unique optical properties of metal nanoparticles, such as LSPR induced from AuNPs, to enhance fluorescence signals, eliminating the need for extensive

enzyme usage and reducing the associated risks and costs[49-52, 59, 60]. There is immense potential in combining intracellular miRNA detection with MEF techniques to achieve a highly sensitive sensing platform, although only a limited amount of related work has been reported. In light of limited studies on monitoring T cell differentiation from an miRNA perspective and the absence of a cost-effective and sensitive intracellular miRNA probing platform, this study aims to provide an a simple, cost-effective and sensitive MEF sensing platform to intracellularly monitor T cell differentiation.

1.5 Localised Surface Plasmon Resonance (LSPR)

A localised surface plasmon resonance (LSPR) is a collective oscillation of localised electrons at the surface of metal under the condition that the size of the nanoparticle is much smaller than the wavelength of light ($d <<< \lambda$), and such collective oscillation is maximal at the resonance wavelength[51, 52, 61]. For example, silver or gold nanoparticles have been extensively studied because of their high quality of surface plasmon generation and broad absorption range in visible light to near-infrared regions. When the particle is excited by an incident photon, the incident photon interacts strongly with the surface electron and creates a dipole electric field oscillation on the surface of the nanoparticle, as illustrated in Figure 2, resulting in the induction of a strong confined electromagnetic field, also called near-field, near the surface nanoparticles [61]. The enhancement factor can simply be evaluated by the ratio of measured electromagnetic field strength (E) to the reference electromagnetic field (E_0), which is shown in Equation 1 [62]. Such electromagnetic field enhancement contributes to the recent prosperous advancement in surface-enhanced Raman scattering (SERs) and plasmon-enhanced fluorescence (PEF) or so-called metal-enhanced fluorescence (MEF) applications.

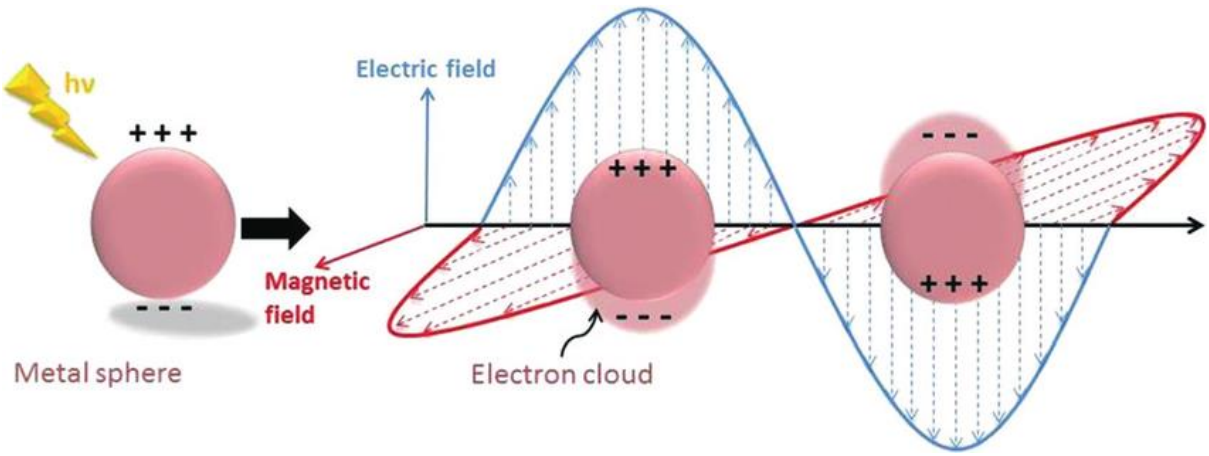

Figure 1. The collective oscillation of electrons after being excited by incident light. The localised electron is pulling back and forth, forming a dipole electric oscillation on the nanoparticle surface [63].

$$\mathrm{EF} = \left(\frac{E}{E_0}\right)^2 \ldots\ldots\ldots\ldots\ldots\ldots\ldots\ldots\ldots\ldots\ldots\ldots \text{(1)}$$

$$\sigma_{ext} = 9\frac{\omega}{c}\varepsilon_{3/2}V_0\frac{\varepsilon_2(\omega)}{[\varepsilon_1(\omega)+2\varepsilon_m]^2+\varepsilon_2(\omega)^2} \ldots\ldots\ldots \text{(2)}$$

The Drude model describes the relationship of the LSPR oscillating frequency as dependent on the dielectric environment and nanoparticle geometry, while Mie's theory describes the optical extinction of spherical nanoparticles (σ_{ext}) as shown in Equation 2, where V_0 is the volume of spherical nanoparticles ω is the angular frequency of extinction radiation, ε_m is the dielectric function of the medium, $\varepsilon_1$and ε_2 are the real and imaginary parts of the dielectric function of the metal nanoparticles respectively [61]. The optical extinction (adsorption and scattering) of nanoparticles reaches a maximum at LSPR oscillation wavelength, and it is highly confined to the nanoparticle geometry as well as composition [51, 52, 61]. In other words, the nanoparticles exhibit maximum optical adsorption and scattering at LSPR frequency. Therefore, it is possible to achieve optimal optical extinction of nanoparticles at LSPR oscillating frequency by manipulation of the size of nanoparticle and geometry in order to maximise local electric field. However, Drude's model and Mie's theory take the optical extinction of light, nanoparticle size and geometry, as well as dielectric environment factors into consideration without considering the absorption and emission of emitters such as a fluorophore and the effect of the distance between the emitter and nanoparticle which are important factors in MEF platform.

1.6 Metal-Enhanced Fluorescence Mechanism (MEF)

In addition to previously described traditional miRNA detection methods, nanomaterial and nucleic acid amplification-based detection have been widely explored to facilitate miRNA detection. One of the promising approaches is to utilise metal-enhanced fluorescence for intracellular (MEF) miRNA probing. Metal-enhanced fluorescence (MEF) refers to the enhancement of fluorescence intensity by utilizing metal nanoparticles that can generate localised surface plasmon, such as gold nanoparticles (AuNP). At the LSPR oscillation frequency, the induced strong electric field at the surface of nanoparticles, also called a near field, interacts with fluorophores at its absorption and emission wavelength, which can increase the excitation rate of the fluorophore and its quantum yield, resulting in enhancement of fluorescence intensity.[64] Such interaction amplifies fluorescence intensity in several orders stronger in magnitude. The excitation rate of a fluorophore (γ_e) proportional to electrical field - (E) at the absorption wavelength (λ_{ab}) which is explained by Maxwell's equation with considering fluorophore absorption (μ_{ab}) as shown in Equation 3.[51] The equation supports that the excitation rate of the fluorophore is facilitated by the enhanced electric field coupling with the maximum absorption of the fluorophore at the LSPR oscillation frequency, leading to higher fluorescence intensity.

$$\gamma_e \propto |E \cdot \mu_{ab}|^2 \ldots\ldots\ldots\ldots\ldots\ldots \quad (3)$$

$$\eta = \frac{\frac{\gamma_r}{\gamma_r^0}}{\frac{\gamma_r}{\gamma_r^0}+\frac{\gamma_{abs}}{\gamma_r^0}+\frac{(1-\eta^0)}{\eta^0}} \ldots\ldots\ldots\ldots\ldots\ldots \quad (4)$$

$$\phi = \frac{\gamma_e}{\gamma_e^0} \cdot \eta \ldots\ldots\ldots\ldots\ldots\ldots\ldots \quad (5)$$

After excitation by the incident light, the fluorophore returns to the ground state at a radiative decay rate (γ_r) or at a nonradiative decay rate (γ_{nr}). The quantum yield (η) is modified by the increased local density of optical states at emission wavelength of the fluorophore induced by the enhanced electric field, which is expressed in Equation 4, where γ_r^0 is the intrinsic radiative decay rate, γ_{nr}^0 is the non-intrinsic radiative decay rate, γ_{abs} is metal-enhanced nonradiative decay rate and η^0 is intrinsic quantum yield.[51] After considering both the excitation rate of the fluorophore and its quantum yield, the fluorescence enhancement ϕ can be expressed as Equation 5.[64] The equation demonstrates that the fluorescence enhancement is the product of

the excitation rate of the fluorophore and its quantum yield. Therefore, these studies present a feasibility that fluorescence intensity can be enhanced by facilitating the excitation rate of the fluorophore and its quantum yield at the LSPR frequency of the nanoparticles.

In addition to the intensity of induced electromagnetic field strength, size and geometry of nanoparticles and optical extinction of incident light, the distance between fluorophore and nanoparticle would be another dominating factor to MEF applications. When the distance between nanoparticles and a fluorophore is short enough (quenching region), the quenching effect would be dominant due to Förster resonance energy transfer (FRET); therefore, the metal-enhanced nonradiative decay rate competes with the radiative decay rate as well as the excitation decay rate of the fluorophore and quantum yield decrease.[51] Another study conducted by Kang et al. suggested that the quenching effect was contributed by the reduction of the ratio of the radiative to nonradiative decay rate and the quantum yield of the fluorophore by dipole energy surrounding the nanoparticles.[62] When the distance between nanoparticles and a fluorophore increases but is limited to the effective region of localised surface plasmon (enhancing region), the LSPR effect is dominant, and the fluorescence intensity is enhanced due to the strong induced electric field.[51] A recent study presented that the quenching region was around 2 nm to 5 nm while the enhancing region was around 5 nm to 20 nm, which were highly dependent on nanoparticle size.[49] For instance, Jennings and his colleagues demonstrated that the Cy3 and Cy5 were highly quenched at 2 nm to the surface of 1.5 nm AuNP, indicating that the quenching region should be optimised at around 2 nm.[65] Choi and his team reported that the fluorescence intensity reached maximum when the separation distance was around the length of 21-base-pair double-strand DNA between AuNP with a diameter of 20 nm and a FITC dye.[66] Hence, it is possible to optimise the distance between nanoparticles and a fluorophore to achieve enhanced fluorescence signals. The optimal range for this distance concerning AuNPs typically falls within the range of approximately 5 to 20 nm.

1.7 Project Aim

The primary aim of our research project is to design and develop a metal-enhanced fluorescence-based nanoprobe for the detection of intracellular miRNA-21 and miRNA-150 within cytotoxic $CD8^+$ T cell subsets at various stages of activation, ranging from a naïve to an activated state. Our approach focuses on precise control of the separation distance between the fluorophore and metal nanoparticles, taking into consideration the near-field enhancement region. By strategically manipulating this distance, we aim to create a nanoprobe with a distinct contrast between signals from miRNA targets (positive) and those without the targets (negative). This strategy fully harnesses the unique properties of metal nanoparticles, such as gold nanoparticles, in conjunction with the fluorophore and the near-field enhancement effect. Notably, this nanoprobe design obviates the need for additional nucleic acid amplification steps, relying solely on the strategic adjustment of the separation distance between the fluorophore and the nanoparticles, offering a simple, cost-effective method for miRNA intracellular detection.

1.8 Detection Scheme

The sensing schematic of the metal-enhanced fluorescent (MEF) nanoprobe for the detection of miR-21 and miR-150 in $CD8^+$ T cell study was illustrated in Scheme 1. The gold core nanoparticle induces a strong near field at the LSPR oscillation frequency interacting with fluorophore at its absorption and emission wavelength. Such interaction amplifies fluorescence intensity in several folds stronger in magnitude[64]. The silica shell coating acts as a precisely controlled spacer between the gold core nanoparticle and the fluorophores in order to optimise the enhancement effect. In this study, four different silica shell thicknesses were fabricated to investigate the MEF effect regarding the distance between the fluorophore and AuNP. Moreover, two organic fluorescent dyes were chosen to investigate the MEF effect and to label miRNA-150 and miRNA-21, namely, fluorescein isothiocyanate (FITC) and rhodamine B isothiocyanate (RITC). The absorption and emission peaks for FITC are 485 nm and 520 nm, and RITC are 560 nm and 580 nm, respectively. These two fluorophores were covalently bonded on the amine-functionalized silica shell of the AuNP by a coupling reaction of isothiocyanate and amine group. The second silica shell was further coated on nanoparticles and then functionalised with an amine group by APTEs for DNA modification by using SMCC, which was a heterobifunctional linker. The nanoparticle was absorbed onto graphene oxide (GO), mainly by π-π stacking interaction, which was an excellent quencher to quench fluorescence signal. Equal amounts of FITC-coated and RITC-coated $AuSiO_2$ nanoprobes were pre-mixed with GO to form a multiplex sensing platform. The FITC-coated and RITC-coated $AuSiO_2$ were designed to probe miR-150 and miR-21, respectively. In the presence of target miRNA, the fluorescence signal is restored according to the concentration changes of target miRNA.

To investigate the expression level changes of interested miRNA in $CD8^+$ T cell subsets, the designed nanoprobes were delivered into $CD8^+$T cell, extracted from 6-7 weeks old C57BL/6 male mice, before activation for naïve cell, and after activation for effector and memory T cells. Confocal images were taken on day 0, day 1, day 3, day 5 and day 7, respectively, to monitor fluorescence intensity changes for miRNA expression monitoring. Flow cytometry and qRT-PCR were performed to validate expression level changes of miRNA in T cell subsets.

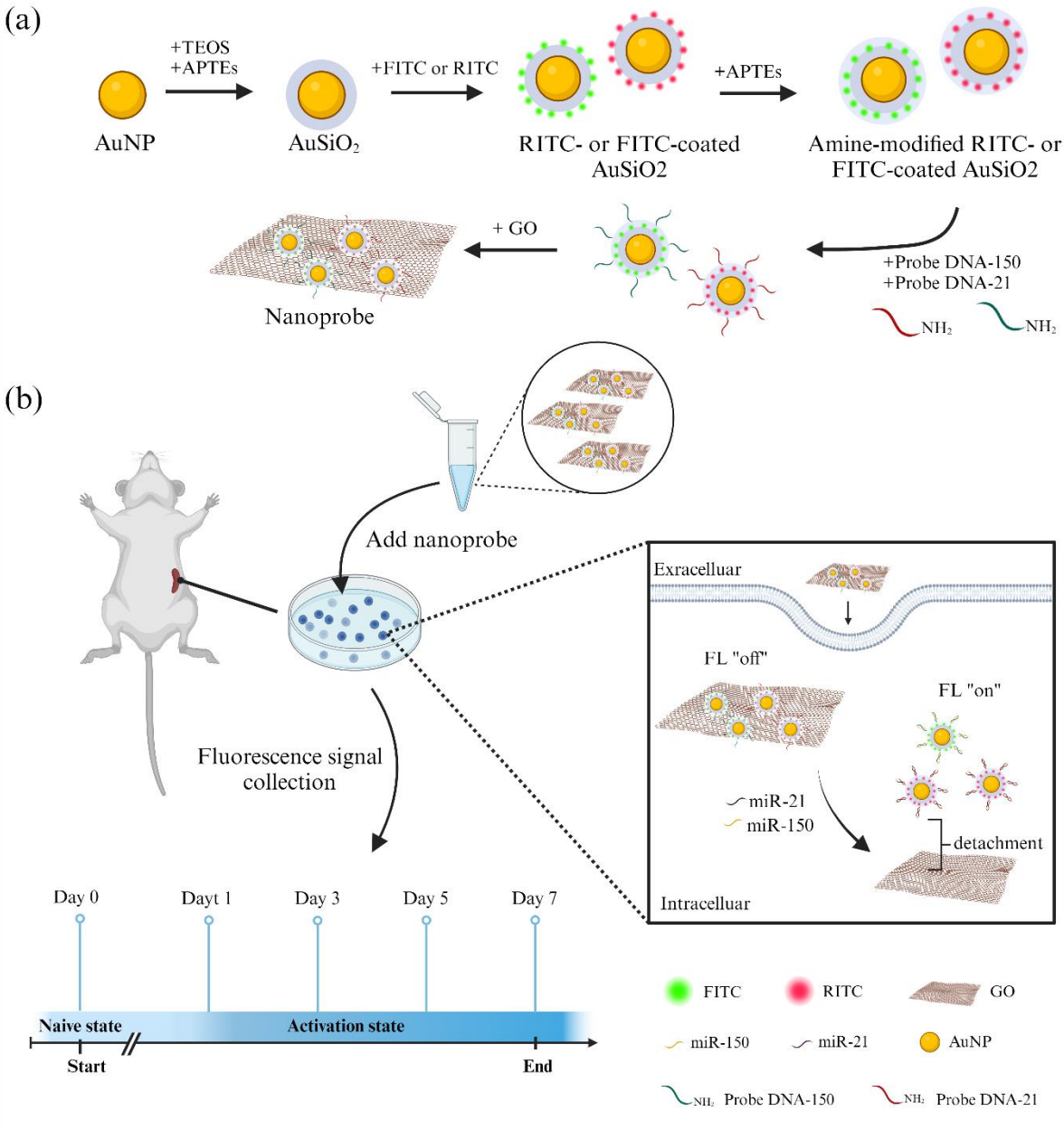

Scheme 1. Schematic illustration of the MEF detection platform. (a) Fabrication process of MEF nanoprobe. (b) Schematic drawing of the MEF sensing flow

Chapter 2 Methodology

2.1 Materials and Chemicals

N,N-Dimethylformamide (DMF), magnesium chloride ($MgCl_2$), sodium chloride (NaCl) were purchased from Aladdin Industrial Corporation (Shanghai, China). Fluorescein isothiocyanate (FITC) and rhodamine B isothiocyanate (RITC) were purchased from Rhawn Company (Shanghai, China). 3-aminopropyl)triethoxysilane (APTEs, 99%), tris(2-carboxyethyl)phosphine hydrochloride (TCEP), tetraethyl orthosilicate (TEOS,98%), gold(III) chloride trihydrate ($HAuCl_4 \cdot H2O$) and tri-sodium citrate dihydrate ($HOC(COONa)(CH2COONa)2 \cdot 2H2O$) were purchased from Sigma-Aldrich Chemicals Company (US). Succinimidyl-4-(N-maleimidomethyl)cyclohexane-1-carboxylate (SMCC), Tris-EDTA (pH 7.0, RNase-free), Tris-EDTA (pH 8.0, RNase-free), 10X UltraPure™ TBE buffer, TE RNase-free Buffer pH 8.0, UltraPure™ DNase/RNase-free distilled water and Roswell Park Memorial Institute (RPMI) 1640 Medium were purchased from Thermo Fisher Scientific (Hong Kong) Limited. The DNA, RNA, primers, miRNA first strand cDNA synthesis (tailing reaction) kit and real-time microRNAs qPCR kit were provided by Sangon Biotech Co., Ltd (Shanghai, China). RNAiso plus was purchased from TaKaRa Biotech Co., Ltd (Dalian, China). Graphene oxide (GO) was supplied by XFNano Materials Tech Co., Ltd (Nanjing, China). Deionized water (18.2 MΩ) was used throughout the experiment which was purified by Milli-Q system at room temperature. All oligonucleotides were purchased from Sangon Biotech (Shanghai, China) which was purified by HPLC.

2.2 Instrumentation

Absorption spectra was obtained using an ultraviolet-visible spectrophotometer (UV-vis, Ultrospec 2100 pro). Size and zeta potential were collected using a dynamic light scattering analyser (DLS analyser, Zetasizer Nano ZS). Fluorescence intensity was measured using fluorescence spectroscopy (Thermo Scientific Varioskan LUX Multimode Microplate Reader and TECAN Automated Liquid Handling System EVO100). Gold nanoparticles morphology and characterisation were obtained by transmission electron microscopy (TEM, JEOL Model JEM-2010). TEM image was processed by a Java-based image processing program developed at the National Institutes of Health and the Laboratory for Optical and Computational

Instrumentation from the University of Wisconsin (ImageJ). Flow cytometry analysis was performed using BD Accuri C6 Flow Cytometer, and data analyses were conducted using Flow Jo software. qRT-PCR was carried out with a CFX96 Real-Time PCR Detection System (Bio-Rad). Confocal images were acquired with a Leica SPE confocal microscope (Leica Microsystems). Data analysis was performed by using OriginLab and GraphPad.

2.3 Synthesis of Citrate-stabilized AuNP

Gold nanoparticles (AuNPs) with a diameter of 40 nm were prepared using a kinetically controlled seeded growth method according to a previously published study [67]. In this method, 28.9 mL of deionised water (DI) was brought to a boil at 100 C° under reflux with vigorous stirring. Subsequently, 1.1 mL of a 60 mM sodium citrate solution and 0.2 mL of a 25 mM HAuCl4 solution were added to the boiling DI water with continuous stirring over a 15-minute period. After each addition, the boiling mixture gradually cooled and was maintained at 90°C. To further grow the nanoparticles, 0.2 mL of a 25 mM HAuCl4 solution was introduced into the reaction mixture, which was stirred vigorously for 30 minutes. Another 0.2 mL of a 25 mM HAuCl4 solution was introduced and stirred vigorously for 30 minutes to finish the first cycle. 11 mL of the reaction mixture was extracted. The second cycle commenced with the addition of 10.6 mL of DI water, followed by the introduction of 0.4 mL of a 60 mM sodium citrate solution to the reaction mixture. Once again, 0.2 mL of a 25 mM HAuCl4 solution was added with 30 minutes of vigorous stirring, and this step was repeated twice to complete the second cycle. This cyclic process could be reiterated until the desired size of AuNPs was achieved. The 11 mL solution obtained at the end of each cycle was subjected to further characterisation through UV-visible spectroscopy and dynamic light scattering (DLS) measurements to assess the size and size distribution of the synthesised nanoparticles. The citrate-stabilized AuNPs were stored in darkness at 4°C. The morphology of the citrated-capped AuNPs was characterised by TEM, and the mean diameter was determined by analyzing 200 individual nanoparticles across multiple TEM images using ImageJ.

2.4 Synthesis of $AuSiO_2$ Nanoparticles

After the successful synthesis of the AuNPs core, a thin layer of thiol PEG was coated onto the AuNP surface. Subsequently, the AuNPs were transferred into absolute ethanol in order to prevent from AuNPs aggregation [68]. The key function of the thiol PEG was to interact directly with the surface of the AuNPs via thiol adsorption onto the reduced gold surface, resulting in the formation of an Au-S bond, as proposed by Ron et al. [69]. Such a thin layer of PEG can protect AuNPs from aggregation before transferring into absolute ethanol for silica shell growth via a modified Stober method [70]. Thiolated mPEG with a molecular weight of 5000 (0.5 mg/mL, 500 µL) was mixed with 1 mL of a 0.18 nM AuNPs solution and subjected to 45 minutes of sonication. Subsequently, the solution mixture was washed by centrifugation at 6300 rpm for 20 minutes before resuspended in absolute ethanol. This washing step was repeated three times using ethanol and then twice using deionised water with lower centrifuge speeds at approximately 6100 rpm for 15 minutes each time. Following the final wash, the sample was dispersed into 250 µL of deionised water and sonicated for an additional 15 minutes to ensure monodispersion. It was then mixed with a growth solution composed of 985 µL of ethanol, varying volumes of TEOS (0.1, 0.2, 0.6, 1 µL), and 16 µL of a 25% ammonia solution. The resulting solution mixture was vigorously stirred for 44 hours at room temperature. After this growth period, the sample underwent further purification through centrifugation at 6100 rpm for 15 minutes. This washing step was repeated three times using ethanol and then twice using deionised water. Finally, the sample was stored at 4°C until use.

2.5 Synthesis of FITC-coated and RITC-coated $AuSiO_2$ Nanoparticles.

FITC-coated and RITC-coated $AuSiO_2$ nanoparticles were synthesised following a modified protocol based on a previously reported method [71]. Initially, functionalisation of the $AuSiO_2$ nanoparticles was initiated by introducing amine groups, which was achieved using Aminopropyltriethoxysilane (APTEs). In brief, 1 mL of the $AuSiO_2$ nanoparticle suspension was subjected to thorough washing through centrifugation and subsequent dispersion in absolute ethanol. Subsequently, 2 µL of APTEs was meticulously added to the dispersed $AuSiO_2$ nanoparticles. The solution mixture underwent agitation at 1000 rpm and was allowed to incubate overnight at room temperature. The resulting solution was then subjected to a series of washing steps to ensure the effective functionalisation of amine groups and eliminate excess APTEs. This involved three successive ethanol washes followed by a final wash with deionised

water by centrifugation at approximately 6100 rpm for 15 minutes. Finally, the amine-functionalised $AuSiO_2$ nanoparticles were re-dispersed in ethanol. Regarding fluorescein isothiocyanate (FITC) and Rhodamine B isothiocyanate (RITC) immobilisation on amine-functionalised $AuSiO_2$ nanoparticle, 50ul of FITC and RITC at a concentration of 1 mg/mL were prepared separately in dimethylformamide (DMF). These dye solutions were introduced dropwise into two tubes of 1 mL $AuSiO_2$ nanoparticle suspension separately. The resulting solution mixture was subjected to vigorous shaking at 1000 rpm in a dark environment overnight at room temperature. Subsequently, the FITC-coated and RITC-coated $AuSiO_2$ were washed by centrifugation at 6100 rpm for 15 minutes before resuspended in absolute ethanol. This washing step was repeated three times using ethanol and then twice using deionised water. The nanoparticles were then dispersed in absolute ethanol before undergoing a 20-minute sonication process. Finally, the prepared samples were stored in the darkness at 4°C.

2.6 DNA Functionalization of the Nanoparticles

The sample was carefully shielded from light throughout the following procedure to avoid potential photobleaching of a fluorophore. Amine functionalised FITC-coated and RITC-coated $AuSiO_2$ were freshly prepared before DNA modification. 2 uL APTEs were added into the solution sample, and the solution mixture was subjected to overnight shaking at 1000 rpm at room temperature. The amino-functionalised FITC-coated AuSiO2 and RITC-coated were washed thrice in ethanol and twice in DI water at 6100rpm for 15 minutes and subsequently dispersed in 0.1 M PB buffer (150ml NaCl, pH7.2) for the following DNA modification. Thiol DNA was immobilised covalently onto amine functionalised FITC-coated and RITC-coated $AuSiO_2$ nanoparticles by a heterobifunctional crosslinker, Succinimidyl-4-(N-maleimidomethyl)cyclohexane-1-carboxylate (SMCC). Firstly, To initiate this process, SMCC was dissolved in DMF at a concentration of 3.7 mg/ml and added to the FITC-coated $AuSiO_2$ nanoparticles suspended in 0.1M PB buffer (150ml NaCl, pH 7.2. This solution mixture was agitated at 1000 rpm for 1 hour at room temperature while being kept in the dark. The FITC-coated $AuSiO_2$ nanoparticles were washed twice in PB buffer and subjected to sonification for 10 minutes. Prior to DNA conjugation, the disulfide bond from the thiol DNA was activated using TCEP. The molar ratio of 80 nm FITC-coated and RITC-coated $AuSiO_2$ to thiol DNA was 1:8350, and the molar ratio of TCEP to MB was 200:1. 15 ul thiolated-DNA (100uM) was incubated with 5ul TCEP (100mM) for 1 hour at room temperature under shaking at 1000rpm.

The FITC-coated and RITC-coated $AuSiO_2$ were mixed with pre-treated DNA-150/TCEP and DNA-21 solution, respectively, under shaking at 1000rpm for 4 hours at room temperature in the dark. Excess DNA was eliminated by centrifugation at 6100rpm twice in ultrapure water and stored in the dark at 4 C° until further use.

2.7 Quenching and Kinetics Studies

0.05 nM of the nanoprobe was mixed with different volumes of GO (1mg/ml) in DI water and prepared in triplicate. The final concentration of GO in a 40ul vial includes 20, 40, 60, 80, 100, 120, 140, 160, 180 and 200 µg/ml. The sample solution was allowed to incubate at room temperature for 30 minutes before fluorescent intensity measurement. For kinetic studies, 0.05 nM of nanoprobe was hybridised with 10nM complementary target miRNA-21 and miRNA-150, respectively, and the fluorescence intensity was measured every 10 minutes seven times to determine the fluorescence signal recovery time. This time-course analysis was conducted to determine the recovery time of the fluorescence signal, shedding light on the kinetics of the nanoprobe's response to the presence of complementary DNA targets.

2.8 Sensitivity, Selectivity and Stability Studies

The sensitivity of the nanoprobe was analysed by incubating various concentrations of complementary target miRNA-21 and miRNA-150, respectively. 0.05 nM of nanoprobes were hybridised with varying concentrations of the complementary target miRNA (0, 0.1, 0.2,0.5, 1, 5, 10nM) in TE buffer at pH 7.2 containing 1mM EDTA, 150mM NaCl and 50mM $MgCl_2$. The sample solution mixture was allowed to incubate at room temperature for 1 hour before fluorescent intensity measurement. The FITC-coated nanoprobe was excited at 485 nm and measured at 520 nm, while the RITC-coated nanoprobe was excited at 650 nm and measured at 670 nm. The fluorescence was measured by a spectrofluorometer and fluorescence microplate reader, and the experiment was conducted in triplicate. The limit of detection (LOD) of the designed nanoprobes was calculated using the equation $LoD = 3\sigma/k$ (where σ is the population standard deviation and k is the slope of the calibration curve). For the selectivity study, 10 nM of scrambled DNA were hybridised with 0.05 nM of nanoprobes in TE buffer containing 1 mM EDTA, 150 mM NaCl and 50 mM $MgCl_2$ at pH 7.2. The solution mixture

was heated up to 75 °C for 5 minutes, followed by slowly cooling down to room temperature and allowing 2-hour incubation. The fluorescence intensity was measured by the fluorescence microplate reader, and the experiment was conducted in triplicate. For the stability study, 0.05 nM of FITC-coated and RITC-coated $AuSiO_2$ nanoparticles were suspended in two buffers, namely, TE buffer (containing 1 mM EDTA, 150 mM NaCl and 50 mM $MgCl_2$ at pH 7.2) and cell growth medium (Roswell Park Memorial Institute (RPMI) 1640 medium supplemented with 10% fetal bovine serum (FBS)and 1% (100IU/ml) antibiotics penicillin/streptomycin). Fluorescent signal was collected on day 1, day 2, day 3, day 4, day 7, day 14 and day 21.

2.9 $CD8^+$ T cell Collection and Sorting

6-7 weeks old C57BL/6 male mice weighing between 18-20g were procured from the Central Animals Faculty of Hong Kong Polytechnic University. All mice were housed under pathogen-free conditions at 25 °C with unrestricted access to food and water. Animal ethics is strictly followed in all animal experiments. $CD8^+$ T cells were extracted from the spleen of mice after euthanasia by intraperitoneal injection of overdose anaesthetic. The spleen was rinsed with PBS with 1 mM EDTA and ground by a plunger of a 1 mL syringe. $CD8^+$ T naïve cells were collected by MojoSort™ Isolation Kit following the manufacturer's protocol. In brief, cells were first strained through a 70 μm cell strainer and then suspended in a 5 mL pre-cold RPMI 1640 medium. Subsequent centrifugation at 300 xg for 5 minutes allowed for the collection of cells. These collected cells were resuspended into MojoSort™ buffer with an adjusted concentration of 1 x 10^8 cells per mL. Aliquot, 100 uL of the cell suspension, was thoroughly mixed with 10 uL of the Biotin-Antibody Cocktail and allowed to incubate on ice for 15 minutes. Subsequently, 10 uL of Streptavidin nanobeads was added to the solution, which was once again incubated on ice for an additional 15 minutes. For the purification, 2.5 mL of MojoSort™ buffer was introduced to the solution mixture, and the tube containing this mixture was placed on a magnet for 10 minutes. The resulting supernatant solution containing $CD8^+$ T cells was meticulously collected, leaving behind any residual Streptavidin nanobeads. This purification step was performed twice. The cells were sorted directly into RPMI 1640 supplemented with 10% fetal bovine serum (FBS) and 1% (100IU/ml) antibiotics penicillin/streptomycin (Pen/S), ensuring viability and suitability for subsequent experiments.

2.10 Cell Culture and Activation of Primary $CD8^+$ T cells

The collected $CD8^+$ T cells were evenly distributed in a 6-well culture plate. The T cells were activated using dynabeads mouse T-activator CD3/CD28 kit according to the manufacturer's protocol. 2 uL of dynabeads mouse T-activator CD3/CD28 was mixed with 100 uL of purified T cells containing 8 x 10^4 cells in Roswell Park Memorial Institute (RPMI) 1640 medium supplemented with 10% fetal bovine serum (FBS) and 1% (100IU/ml) antibiotics penicillin/streptomycin. Cells were routinely maintained in a humidified chamber at 37 °C and 5% CO_2. Optical images and cell counting were performed on day 0, day 1, day 3, day 5, and day 7. For the control group and naïve sample, no dynabeads were added before qRT-PCT, flow cytometry and confocal images.

2.11 Cytotoxicity Assay

Cytotoxicity assay was performed by using Cell Counting Kit-8 (CCK-8) to study cell viability and to determine the optimal concentration of nanoprobe for intracellular sensing. Naïve T cells were seeded in a 96-well plate, with each well containing 6000 cells. The nanoprobe was dispersed in a cell growth medium by centrifugation at 12000 xg in advance. Various concentrations of nanoprobes ranging from 0.01 nM to 0.05 nM were mixed with 10 uL of CCK-8 solution and incubated with Naïve T cells in a cell growth medium for 4 hours at 37 °C and 5% CO_2. The cells incubated in a cell growth medium without nanoprobes served as a control group. Absorbance was measured promptly at 450 nm using a fluorescence microplate reader. All experiments were carried out in triplicate to ensure the reliability and consistency of the results obtained.

2.12 Confocal Fluorescence Imaging

T cells were seeded at a density of 1.2 x 10^5 cells per 38 mm confocal dish. 0.05 nM of nanoprobe was incubated with the naïve T cells in cell growth medium at 37 C° and 5% CO_2 on day 0, day 1, day 3, day 5, and day 7 for 0.5, 2, 4 and 6 hours. The cells were collected and washed by centrifugation at 1000rpm for 5 minutes twice to remove excessive nanoprobes. The images were captured on day 0, day 1, day 3, day 5, and day 7 by the confocal microscope using 488 nm and 552 nm excitation. The absorption and emission peaks for FITC were at

485nm and 520nm, respectively, while the absorption and emission peaks for RITC were at 560nm and 580nm.

2.13 Flow Cytometry

Flow cytometry was carried out to quantify the intracellular fluorescence intensity of miRNA-150 (Ex=488nm, Em=495-550nm) and miRNA-21(Ex=561, Em=580-650nm). 0.05 nM of nanoprobe, containing 0.025nM of FITC-coated and 0.025nM RITC-coated $AuSiO_2$ nanoparticles mixed with 140 ug/ml GO, which specifically recognised miRNA-150 and miRNA-21 respectively were incubated with naïve and activated $CD8^+$ T cell in cell growth medium (RPMI 1640 containing 10% FBS and 1% Pen/S) for 4 hours at different time points. The cell suspensions were washed and resuspended in 1X PBS containing 1% bovine serum albumin (BSA) and then incubated in the incubator at 37 C° and 5% CO_2 for 30 minutes. This provided sufficient time for cellular uptake. Flow cytometry analysis was performed using BD Accuri C6 Flow Cytometer, and data analyses were conducted using Flow Jo software.

2.14 Quantitative Real-Time Reverse Transcription PCR (qRT-PCR)

To evaluate concentration changes of miRNA-150 and miRNA-21 in different T cell subsets, qRT-PCR was carried out to quantify its expression level. $CD8^+$ T cells were extracted from the spleen of mice and purified by MojoSort™ Isolation Kits. Cells were equally seeded in a 6-well microplate. For the naïve T cell sample at day 0, total RNA was directly extracted and reverse transcribed into cDNA without activation. In order to monitor miRNA changes in T cell subsets, naïve T cell was activated by Dynabeads Mouse T-Activator CD3/CD28 at day 0 and allowed to further differentiate in a humidified chamber at 37 °C and 5% CO_2. Subsequently, total RNA was extracted by using RNAiso Plus on day 1, day 3, day 5 and day 7, and reverse transcribed into cDNA.

Specifically, total RNA was extracted by RNAiso plus (TaKaRa Biotech Co., Ltd Ltd, China) on day 0, 1, 3, 5 and 7. 2 μl total of total RNA was reverse transcribed to cDNA using miRNA First Strand cDNA Synthesis Tailing Reaction kits (Sangon Biotech Co., Ltd, China) at day0, day1, day3, day5 and day7 according to manufacturer's protocol under the following condition: 37 °C for 60 minutes and 85°C for 5 minutes. qRT-PCR was performed using a Real-time

microRNAs qPCR kit (Sangon Biotech Co., Ltd, China) according to the manufacturer's protocol. The thermal cycler conditions consisted of one cycle of denaturation at 95°C for 30 seconds followed by 40 cycles of 95°C for 5 seconds and 60°C for 30 seconds. The relative expression levels of miRNA-21 and miRNA-150 were calculated by the Ct value and normalised to U6 small nuclear RNA expression due to its high expression level and independence of $CD8_+$ T cell differentiation status. The relative change of gene expression level was calculated by $2^{-\Delta\Delta Ct,}$ and the experiment was performed in triplicate. The primer sequences used are listed in Table 2.

Table 2 The sequence information of DNA

Name	Sequence (5′ – 3′)
miRNA-21 probe	TCA ACA TCA GTC TGA TAA GCT A -C6-SH
miRNA-150 probe	CAC TGG TAC AAG GGT TGG GAG A -C6-SH
miRNA-21	TAG CTT ATC AGA CTG ATG TTG A
miRNA-150	TCT CCC AAC CCT TGT ACC AGT G
scramble miRNA-21	GCA TCG CAT TAG TAA TAT GTT G
scramble miRNA-150	ATC AGA CTT CGC GCA CTT CTC C
miRNA-21 forward primer	AGC TTA TCA GAC TGA TGT TG
miRNA-21 reverse primer	GAA CAT GTC TGC GTA TCT C
miRNA-150 forward primer	CTC CCA ACC CTT GTA CCA
miRNA-150 reverse primer	GAA CAT GTC TGC GTA TCT C
U6 forward primer	GCT TCG GCA GCA CAT ATA CTA AAA T
U6 reverse primer	CGC TTA CGA ATT CGT GTC AT

Chapter 3 Results and Discussion

3.1 Synthesis and Characterization of AuSiO2

Prior to the synthesis of gold-silica core-shell particles($AuSiO_2$), stable citrated-capped AuNPs were first successfully prepared by using a previously reported kinetically controlled seeded growth method[67]. These AuNPs served as the core material for subsequent modifications. The morphology of the citrated-capped AuNPs was demonstrated by TEM, revealing a uniform particle size distribution with a mean diameter of 41.7 ± 3.8 nm (Figure 2a). The optical properties of the AuNPs were further elucidated through UV-vis. The resulting absorption spectrum exhibited a prominent light extinction peak at approximately 530 nm (Figure 2b). Additionally, the zeta potential of the AuNPs was determined to be approximately -33 ± 1.2 mV (Figure 1d). DLS analysis corroborated the TEM findings, with the average hydrodynamic diameter of the AuNPs measuring around 43 nm (Figure 2c). This consistency between the TEM and DLS results confirms the successful preparation of the AuNPs. The concentration of the AuNPs was quantified using a method based on the ratio of the absorption at 450 nm to the corresponding molar decadic extinction coefficient for AuNP with a diameter of 42 nm (5.74 x 10^9 M^{-1} cm^{-1}), as established by Haiss et al.[72]. The concentration of the AuNPs was determined to be 0.8 nM. These comprehensive characterisations validate the successful generation of stable citrate-capped AuNPs, thereby establishing the foundation for the subsequent fabrication of gold-silica core-shell particles ($AuSiO_2$).

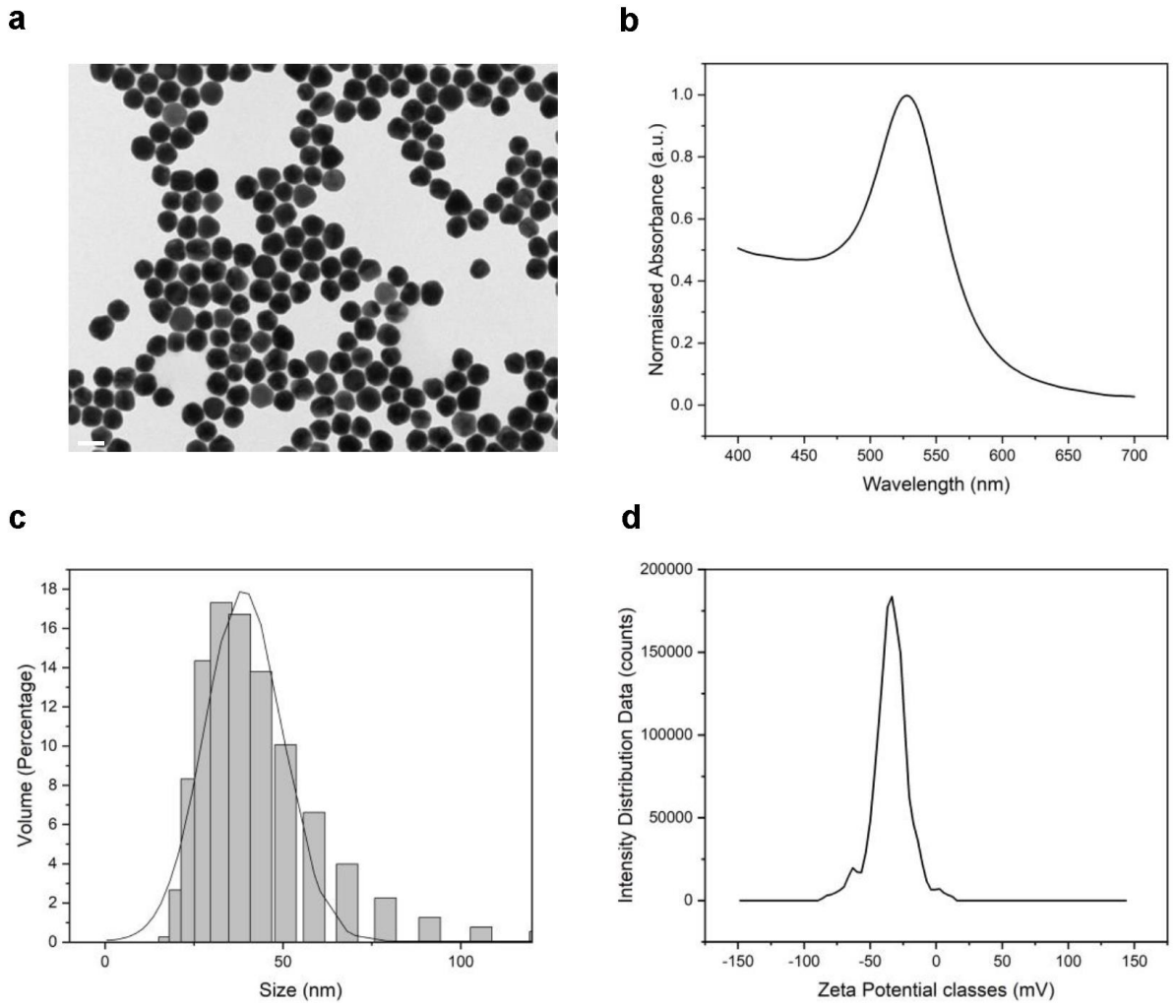

Figure 2. Characterisation of citrated-capped AuNPs. (a) TEM image of citrated-capped AuNPs. The diameter of AuNP was 41.7 ± 3.8nm. Scale bar: 50 nm (b). Normalised UV-vis spectra of citrate-capped AuNPs. The extinction peak of AuNP was at around 530nm. (c) The Zeta potential of AuNPs was around -33mV. (d) DLS distribution of AuNPs was centred at 43nm

After the successful synthesis of the AuNPs core, a thin layer of thiol PEG was coated onto the AuNP surface before transferring AuNPs into absolute ethanol[68]. The PEG coating on AuNPs provides steric hindrance which shield the surface of particles from aggregation, leading to enhanced stability of gold nanoparticles in absolute ethanol. This protective coating was essential to prevent the aggregation of AuNPs. The primary role of thiol PEG was to interact directly with the AuNP surface, facilitating thiol adsorption onto the reduced gold surface and resulting in the formation of stable Au-S bonds, as proposed by Ron et al.[69]. This thin PEG layer effectively shielded the AuNPs from aggregation before they were transferred into absolute ethanol, preparing them for the subsequent growth of a silica shell using a modified

Stober method[70]. The formation of the silica shell involved the bonding of silica to the PEG-coated AuNPs through a combination of hydrogen and covalent bonds. This process was achieved through the hydrolysis and condensation of tetraethyl orthosilicate (TEOS) in the presence of ammonia, a procedure commonly referred to as salinisation. Notably, the thickness of the silica shell could be controlled by adjusting the volume of TEOS introduced, with options ranging from 0.1 to 1 μL. Further functionalisation of the $AuSiO_2$ nanoparticles was accomplished by introducing an aminosilane, aminopropyltriethoxysilane (APTEs), into the reaction mixture. This additional modification endowed the $AuSiO_2$ nanoparticles with amine groups for the subsequent fluorophore coating.

The morphological characteristics of amine-modified $AuSiO_2$ nanoparticles, varying in silica shell thicknesses, were subsequently validated through TEM, as illustrated in Figure 3a. This analysis confirmed the successful synthesis of silica shells with thicknesses of 11 nm, 18 nm, 34 nm, and 45 nm, and specific size details were provided in Table 3. The optical properties of amine-modified $AuSiO_2$ nanoparticles displayed a gradual shift in their light extinction peak from 530 nm to 546 nm, signifying a subtle red shift attributed to the differing thicknesses of the silica shell (Figure 3b). Notably, the inset image in Figure 3b revealed no significant colour variations between the bare AuNPs and $AuSiO_2$ particles with varying shell thicknesses. The zeta potential of the particles underwent distinctive alterations throughout the synthesis process. Initially, the zeta potential was highly negative, approximately -32.4 ± 0.65 mV, owing to the presence of citrate ions on the surface of the unmodified gold nanoparticles. After the coating with PEG polymer, the zeta potential shifted to a slightly negative value, approximately -3.00 ± 0.42 mV. Subsequent salinisation of TEOS led to a reversion of the zeta potential to a highly negative state, approximately -32.9 ± 2.49 mV, due to the dissociation of silanol groups (Si-OH). Finally, upon functionalisation with APTEs, the zeta potential transitioned to a highly positive value, around +25.3 ± 2.69 mV, attributed to the presence of amine groups (Figure 3c). These dynamic alterations in zeta potential profiles delineate the different stages of particle development during the synthesis process and underscore the successful preparation of the $AuSiO_2$ nanoparticles.

The $AuSiO_2$ were coated with two organic fluorescent dyes, namely, FITC and RITC. The isothiocyanate group from these dyes reacted with amino groups, which were pre-treated on

the $AuSiO_2$ nanoparticles. Subsequently, a secondary layer of silica coating was applied to the FITC-coated and RITC-coated $AuSiO_2$ by using APTEs forming amine functionalised FITC-coated and RITC-coated $AuSiO_2$ nanoparticles for the following DNA modification. The thiol DNA was immobilised via a heterobifunctional crosslinker, SMCC. The SMCC contained an NHS ester, which reacted to the primary amine group from the particles and an N-maleimide group reacted to the thiol group from the thiolate DNA. After immobilising DNA, which specifically recognised miRNA-21 and miRNA-150 onto the particles, graphene oxide (GO) was introduced into the platform. In the absence of target miRNA, the nanoprobes were absorbed onto the GO mainly by π-π stacking interaction. Figure 3d illustrated two DNA-modified amine-functionalised FITC-coated and RITC-coated $AuSiO_2$ nanoparticles that were absorbed onto a GO and formed a multiplex sensing platform, which was captured by TEM in Figure 3d. It underscores the successful fabrication of the FITC-coated and RITC-coated $AuSiO_2$ sensing platform.

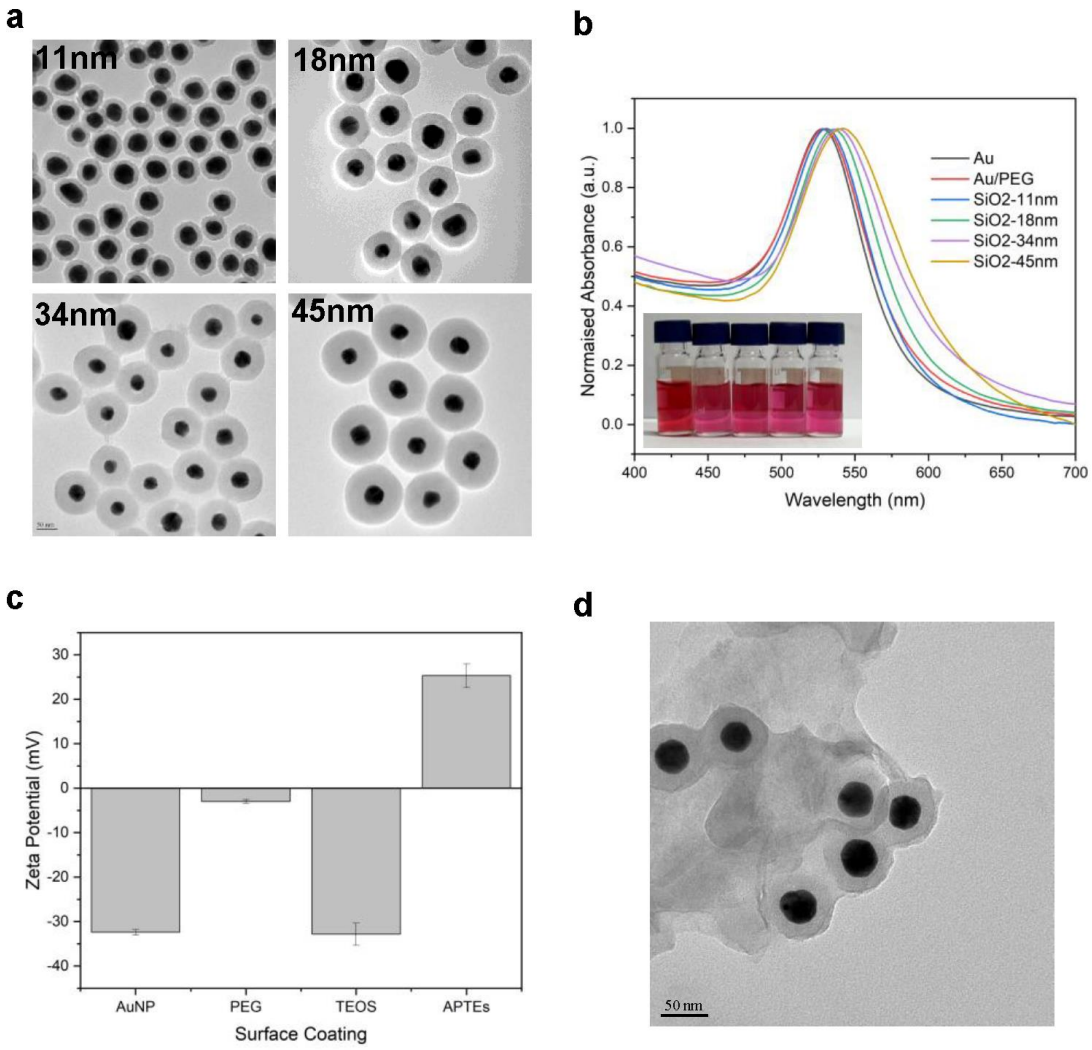

Figure 3. Characterisation of $AuSiO_2$ nanoparticles. (a) TEM images of $AuSiO_2$ nanoparticles with various silica shell thicknesses, including 11 nm, 18 nm, 34 nm, and 45 nm. Scale bar: 50 nm. (b) Normalised UV-vis spectra of nanoparticles of citrate-capped AuNPs, Au/PEG, and $AuSiO_2$ nanoparticles at different silica shells. Inset: Images taken for $AuSiO_2$ nanoparticles with various silica shell thicknesses. (c) Zeta potential changes of $AuSiO_2$ with different surface coating. Zeta potential was expressed as mean ± SD (n=3). (d) TEM images of $AuSiO_2$ nanoprobe with GO. Scale bar: 50 nm.

Table 3. Diameter of $AuSiO_2$ nanoparticle

Sample	Silica shell thickness (nm)	Final diameter (nm)
AuNPs	0	41.7 + 3.8
$AuSiO_2$-11	11.3 ± 1.2	62 ± 3.2
$AuSiO_2$-18	17.7 ± 1.5	76 ± 4.8
$AuSiO_2$-34	34.4 ± 1.2	104 ± 3.3
$AuSiO_2$-45	45.01 ± 2.6	133 ± 5.9

3.2 Metal Fluorescent Enhancement Effect

In this study, two organic fluorescent dyes were chosen to investigate the MEF effect, namely, fluorescein isothiocyanate (FITC) and rhodamine B isothiocyanate (RITC). At the LSPR oscillation frequency, the induced strong near field at the surface of $AuSiO_2$ interacted with fluorophores at its absorption and emission wavelength. Thus, FITC and RITC were chosen to overlap the extinction peak of $AuSiO_2$. FITC dye displayed absorption and emission peaks at 485 nm and 520 nm, respectively, while the RITC dye demonstrated absorption and emission peaks at 560 nm and 580 nm, respectively. In Figures 4c & 4d, the emission peak of FITC coincided with the extinction peak of $AuSiO_2$, whereas the absorption peak of RITC coincided with the extinction peak of $AuSiO_2$. In Figure 4a, the fluorescent intensity of both FITC and RITC gradually increased and reached the highest intensity when the shell thickness increased from 11 nm to 18 nm before gradually decreasing when the shell thickness further increased from 18 nm to 45 nm. The background was ethanol, and the control referred to the same amount of free fluorescent dye without $AuSiO_2$ in ethanol.

To investigate the enhancement effect contributed by the separation distance, an equal amount of fluorescence dye was added to the $AuSiO_2$ nanoparticles with varying shell thicknesses, and the fluorescent intensity was collected before any washing steps. By comparing the fluorescence intensity of the free fluorescence dye (control group) to that of the FITC-coated and RITC-coated $AuSiO_2$ nanoparticles, the enhancement factor can be calculated, as presented in Figure 4b. The most pronounced enhancement effect was observed when FITC and RITC

were both at the silica shell thickness of 18 nm. The enhancement reached approximately 2.8 times higher for FITC and 1.8 times higher for RITC compared to the control. This finding highlights the significant contribution of the separation distance between the fluorescent dye and the AuNPs due to the MEF effect. Through optimisation of this distance, the fluorescent signal can be effectively maximised. Consequently, $AuSiO_2$ nanoparticles with an 18 nm shell thickness were selected for subsequent fluorescent sensing and in vitro cell studies.

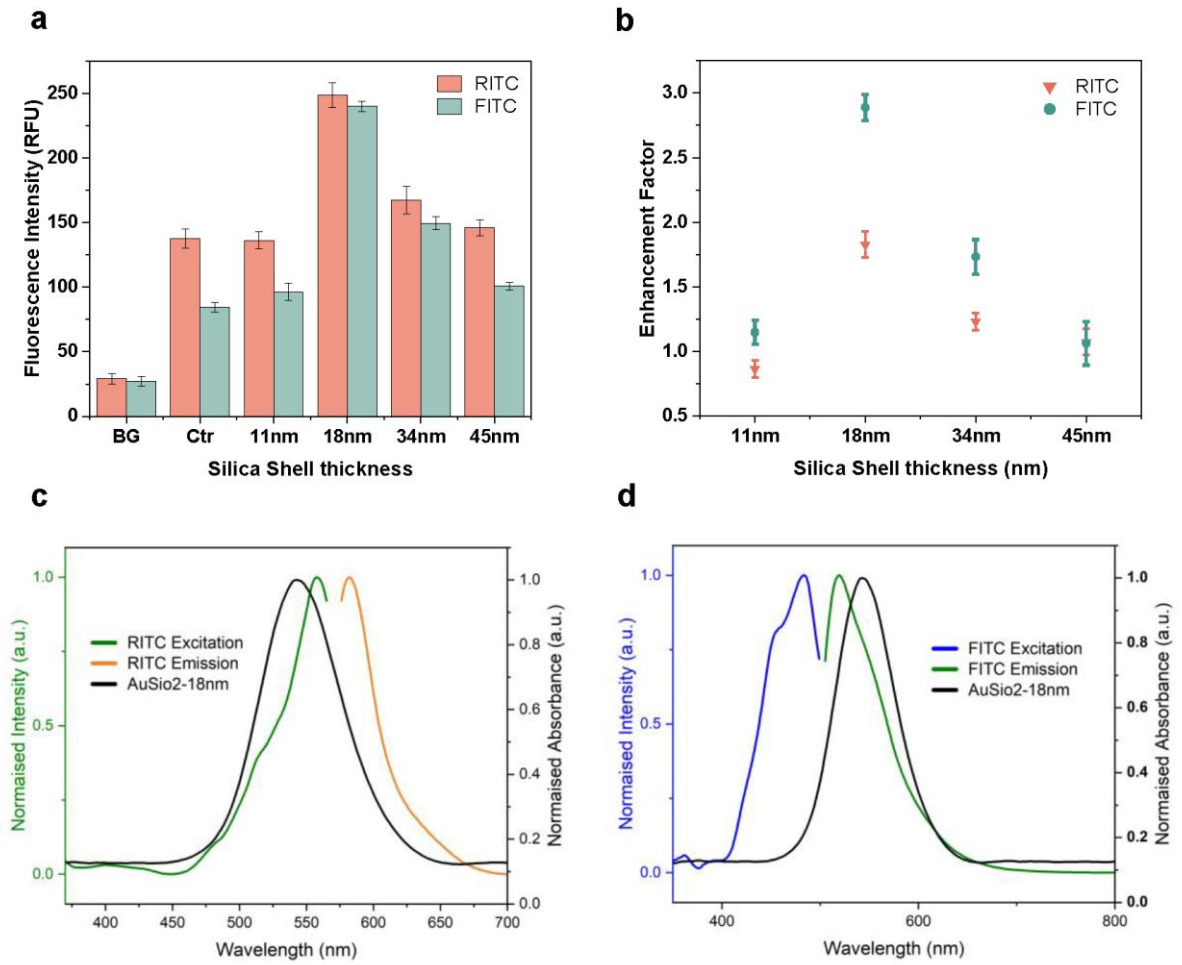

Figure 4. MEF effect of RITC-coated and FITC-coated $AuSiO_2$ nanoparticle. (a) Fluorescent intensity of RITC-coated and FITC-coated $AuSiO_2$ nanoparticles with various silica shell thicknesses in the DI water. The control group was the fluorescent intensity of free RITC and FITC dye at the same concentration. Fluorescent intensity was expressed as mean ± SD (n=9). (b) Fluorescent enhancement factor of RITC-coated nanoparticle at 560nm and FITC-coated nanoparticle at 520nm at various silica shell thickness. Enhancement factors were expressed as mean ± SD (n=9). (c) Fluorescent spectrum of RITC dye and UV-vis spectra of $AuSiO_2$ (18nm silica shell thickness). The Emission peak of the RITC dye overlapped with the extinction peak of the $AuSiO_2$ nanoparticle. (d) Fluorescent spectrum of FITC dye and UV-vis spectra of $AuSiO_2$ (18 nm silica shell thickness). The Excitation peak of the FITC dye overlapped with the extinction peak of the $AuSiO_2$ nanoparticle.

3.3 Fluorescent Sensing

After optimising FITC-coated and RITC-coated $AuSiO_2$ nanoparticles, the quenching effect was then investigated. DNA-modified FITC-coated and RITC-coated $AuSiO_2$ nanoparticles were mixed with various volumes of graphene oxide (GO), and the resulting fluorescent signals were recorded. As depicted in Figure 5a, the quenching efficiency exhibited a sharp increase as the GO concentration increased from 20 μg/ml to 140 μg/ml, ultimately reaching a maximum quenching efficiency of 97% for RITC-coated $AuSiO_2$ nanoparticles and 98% for FITC-coated $AuSiO_2$ nanoparticles after a 30-minute incubation at room temperature. Therefore, the optimal concentration of GO for both FITC-coated and RITC-coated $AuSiO_2$ nanoparticles was determined to be 140 μg/ml, with maximum quenching efficiencies of 98% and 97%, respectively.

To investigate the sensing performance of the nanoprobe, 10 nM of scrambled DNA or target DNA was introduced to the sensing platform in TE buffer at pH 7.2 containing 1mM EDTA, 150 mM NaCl and 50 mM $MgCl_2$ at room temperature for 1 hour. FITC-coated and RITC-coated $AuSiO_2$ nanoprobe were designed to probe for DNA-150 and DNA-21, respectively, and the fluorescence intensities were measured at 520 nm and 580 nm, respectively. Target DNA exhibited significant fluorescence intensity, whereas scrambled DNA showed comparable magnitude to the control fluorescence signal. The control group referred to the negative signal without target DNA. Moreover, the fluorescence intensities were restored around 95.8% for FITC-coated $AuSiO_2$ nanoprobe and 96.1% for RITC-coated $AuSiO_2$ nanoprobe when the target DNA concentration gradually increased to 10 nM (Figure 5b). In addition to the restoring signal-restoring assay, recovery time was also evaluated. Figures 5c and 5d illustrated that the nanoprobe responded steadily to the complementary matched target DNA-150 and DNA-21 in 20 and 30 minutes, respectively. These data confirm that the designed nanoprobe successfully restores the fluorescence signal upon the complementary binding with target DNA sequences, which prompts further investigation into whether the designed sensing platform can restore the fluorescence signal in the presence of target miRNA-150 and miRNA-21 in the T cells.

Furthermore, a concentration-dependent assay was conducted to investigate the sensitivity of the designed sensing platform. Different concentrations of target DNA ranging from 0.1 nM to 10 nM were mixed with the sensing platform in TE buffer at pH 7.2 containing 1 mM EDTA,

150 mM NaCl and 50 mM $MgCl_2$ at room temperature for 1 hour. The fluorescence intensities were highly proportional to the concentration of target DNA-21 and DNA-150 with a R-square values of 0.939 and 0.956, respectively, as illustrated in Figures 6b and 6d. The calculated lowest limit of detection (LoD) for FITC-coated and RITC-coated $AuSiO_2$ nanoprobe was found to be 236 pM and 120 pM, respectively. Notably, these data suggest that the designed nanoprobe can successfully detect target DNA down to the picomolar level without the need for additional amplification steps, thanks to the highly exploitable metal-enhanced fluorescence effect induced by the strong near field. On the other hand, the representation of linear fitting curve showed that the sensing range of our designed nanoprobe is from 0.1pM to 1000pM with a detection limit of 236 and 120 pM. Despite the absence of consensus on the actual concentrations of intracellular miRNA-21 and miRNA-150 due to a lack of standardization and variations in quantification methods, existing studies propose concentrations ranging from 105 to 108 copies per mL (i.e., fM to nM)[73, 74]. The calculated concentration of miRNA-21 and miRNA-150 on day 0 was 31 nM and 47 nM on day 0 for naïve T cells from 1 x 10^6 cells/mL which is consistent to previous studies. Our nanoprobe demonstrates ample analytical sensitivity for effective sensing in this concentration range (i.e., pM level).

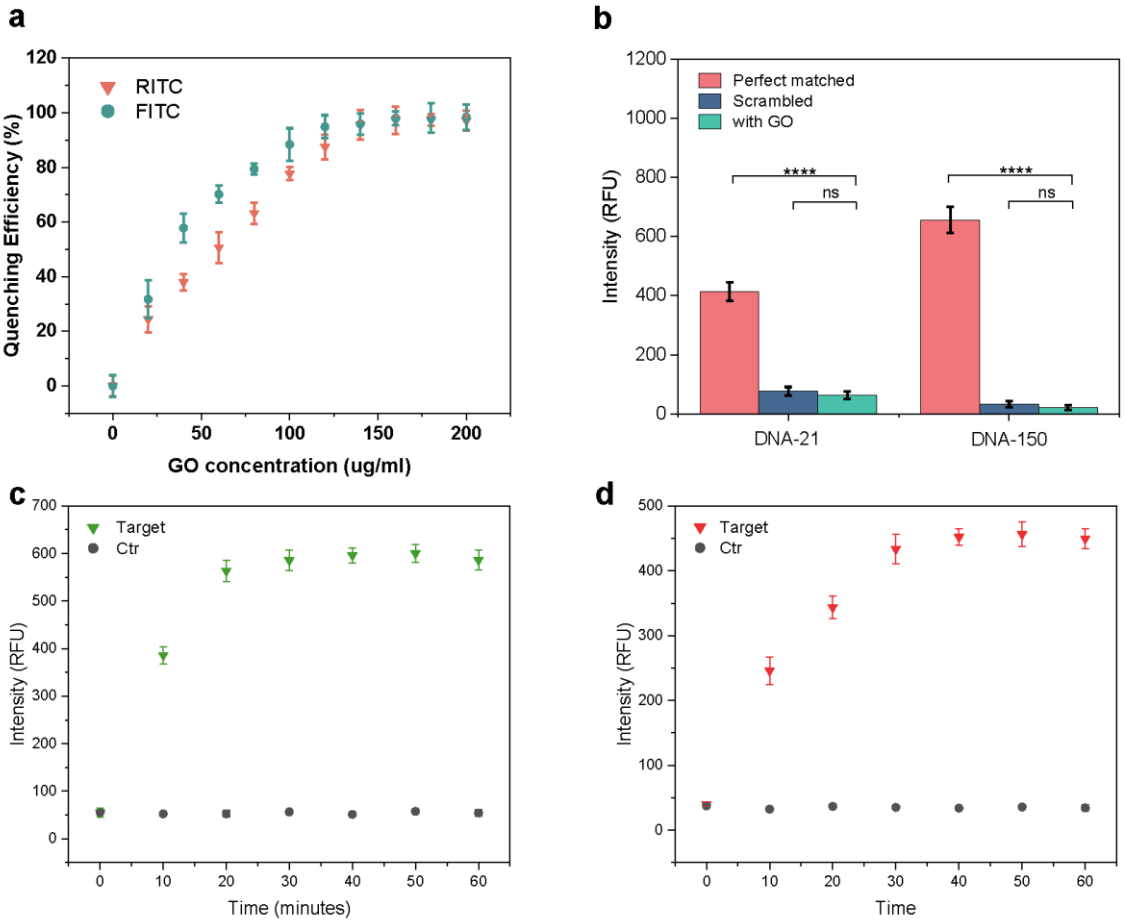

*Figure 5. Fluorescent assay of the designed nanoprobe. (a) Quenching efficiency for RITC-coated and FITC-coated nanoprobe. The fluorescence intensity was measured at 580nm for RITC-coated and at 520nm for FITC-coated nanoprobe in various GO concentrations (0 to 200 ug/ml). Fluorescent intensities were expressed as mean ± SD (n=3). (b) Selectivity. (c) & (d) Recovery time assay of FITC-coated and RITC-coated $AuSiO_2$ nanoprobe. The fluorescent intensity was measured at 580nm for RITC-coated and at 520nm for FITC-coated nanoprobe in 10 nM of target DNA-21 and DNA-150 after 1 hour of incubation at room temperature, respectively. Fluorescent intensities were expressed as mean ± SD). (ns: no significance,p< 0.05, **p< 0.005, *p< 0.0005, and ***p< 0.0001, n= 3, one-way ANOVA test).*

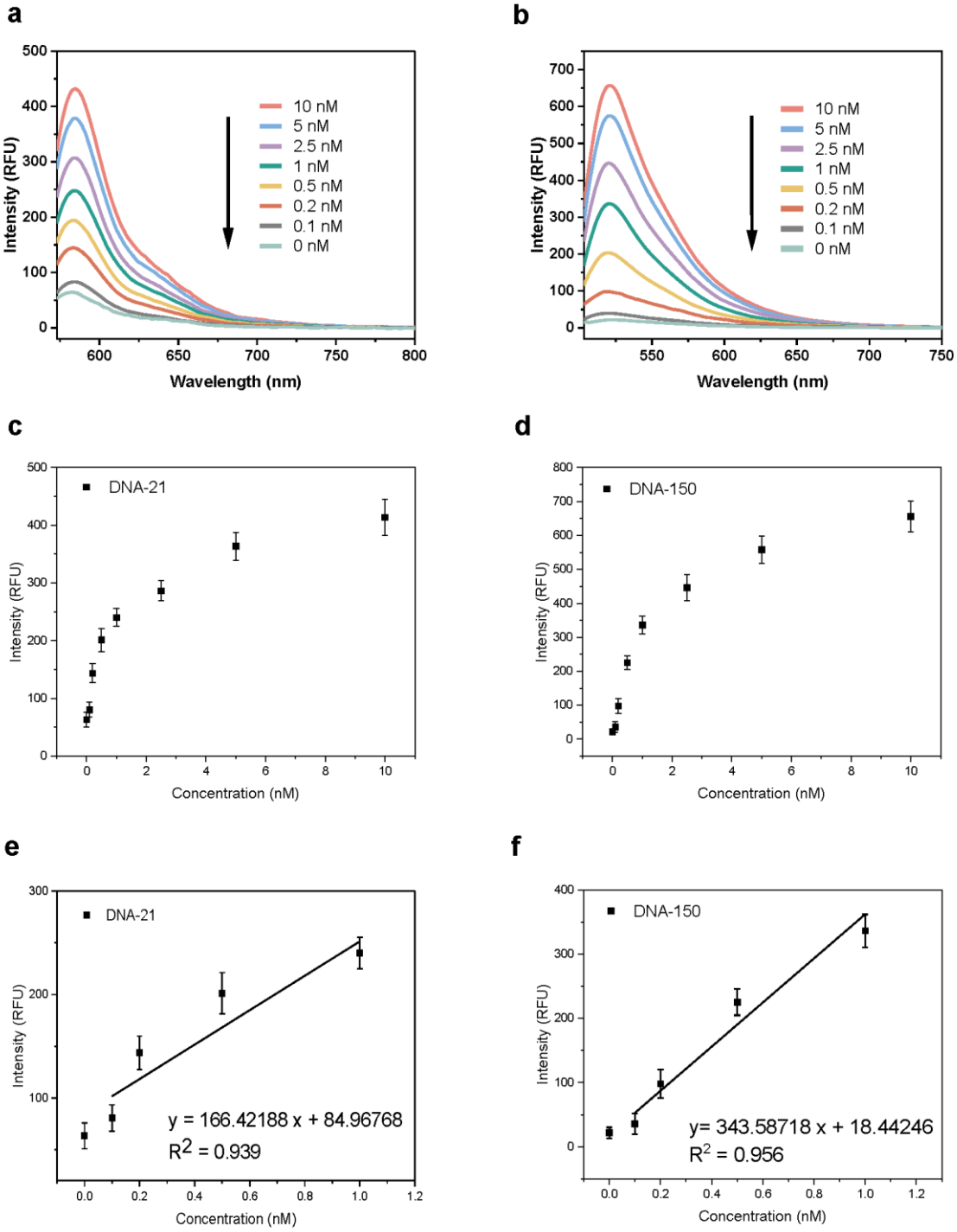

Figure 6. Concentration-dependent assay. (a) Photoluminescence spectra, (c) peak fluorescence intensity, and (e) linear fitting curve of FITC-coated nanoprobe against the increasing concentrations of DNA-21 concentrations ranging from 0.1 to 1 nM (R-square = 0.939, n=3). (b) Photoluminescence spectra and (d) peak fluorescence intensity, and (f) linear fitting curve of RITC-coated nanoprobe against the increasing concentrations of DNA-150 ranging from 0.1 to 1 nM (R-square = 0.956, n=3). Fluorescent intensities were expressed as mean ± SD (n=3).

3.4 Stability Study

To further demonstrate the performance of the sensing platform, a stability test was conducted. The fluorescent intensity of 0.1 nM double silica-shelled FITC-coated and RITC-coated $AuSiO_2$ nanoparticles was measured in different buffers, including TE buffer at pH 7.2 containing 1 mM EDTA, 150 mM NaCl and 50 mM $MgCl_2$ and cell culture medium (RPMI containing 10% FBS and 1% antibiotics penicillin/streptomycin) on day 1, 2, 3, 4, 7, 14, 21. The results showed that the fluorescence intensities remained at 92% in TE buffer and 96% in cell culture medium for double silica-shelled FITC-coated $AuSiO_2$ nanoparticles after 7 days. The fluorescence intensities for double silica-shelled FITC-coated $AuSiO_2$ nanoparticles dropped to 78% and 83% on day 21 in TE buffer and cell culture medium, respectively (Figure 7b). Moreover, double silica-shelled RITC-coated $AuSiO_2$ nanoparticles maintained 90% in TE buffer and 87% in cell culture medium after 7 days and dropped to 74% and 78% on day 21 in TE buffer and cell culture medium, respectively (Figure 7a). Undoubtedly, both double silica-shelled FITC-coated and RITC-coated $AuSiO_2$ nanoparticles demonstrated good stability in both TE pH 7.2 buffer and cell culture medium after 7 days at room temperature. This stability was attributed to the second silica shell layer, which acted as a protective barrier, isolating the fluorescent dyes from environmental factors such as hydrolysis and photobleaching. Notably, the effectiveness of the silica shell protection may depend on the shell thickness and the quality. Consequently, the fluorescence intensity decreased to around 74% to 83% after 21 days. Referring to the TEM image in Figure 2d, the second silica shell thickness was estimated to be approximately 1-2 nm, which acts as an effective and protective layer on the FITC-coated and RITC-coated $AuSiO_2$ nanoparticles. These findings strongly indicate the successful synthesis of double silica-shelled FITC-coated and RITC-coated $AuSiO_2$ nanoparticles, which exhibited a stability of around 90% after a 7-day period.the

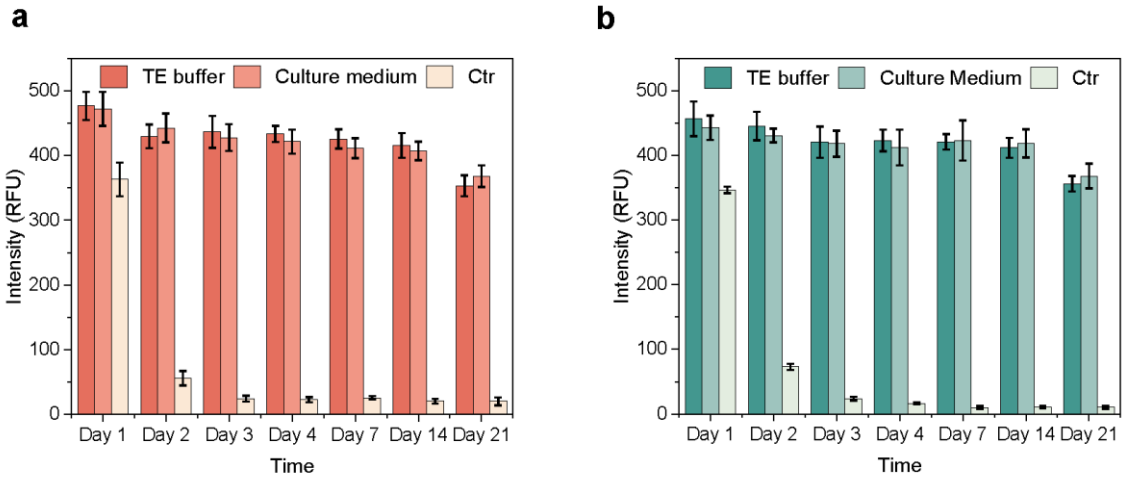

Figure 7. Stability assay. (a) Fluorescent intensity of RITC-coate and (b) and FITC-coated nanoparticles in TE buffer and cell culture medium for three weeks. Fluorescent intensity were expressed as mean ± SD (n=3).

To assess the effectiveness of the second silica shell, a control group consisting of FITC-coated and RITC-coated $AuSiO_2$ nanoparticles without the protective second silica shell was used for comparison (Figure 7a and 7b). The control group showed a significant decline, with both FITC-coated and RITC-coated $AuSiO_2$ nanoparticles maintaining only 20% and 15% of their initial intensities by day 2, respectively. Both further decreased to 6.6% by day 3. Ultimately, both FITC-coated and RITC-coated $AuSiO_2$ nanoparticles without the protective silica shell decreased to approximately 3% of their initial intensities after 7 days. These findings underscored the critical role of the protective second silica shell in maintaining the stability of the fluorescence signal during long-term signal monitoring. It also suggested that a highly stable nanoprobe was successfully prepared.

3.5 Cell Viability Assay

To investigate the potential cytotoxicity of the synthesised nanoprobe, cellular viability was assessed employing the cell counting kit-8 (CCK-8) assay, according to the manufacturer's protocol. Varied concentrations of the nanoprobe were introduced into Naïve T cells and incubated for a duration of 4 hours in a humidified incubator maintained at 37 °C under a 5% CO_2 atmosphere. Subsequently, the absorbance at 450 nm was measured using a microplate reader. As depicted in Figure 8, the cellular viability surpassed 90% after incubation with FITC-coated and RITC-coated $AuSiO_2$ nanoprobes at concentrations ranging from 0.01 nM to 0.05 nM with 140 µg/ ml GO. These results underscore the favourable cellular compatibility of the designed nanoprobes, rendering them conducive for subsequent intracellular investigations.

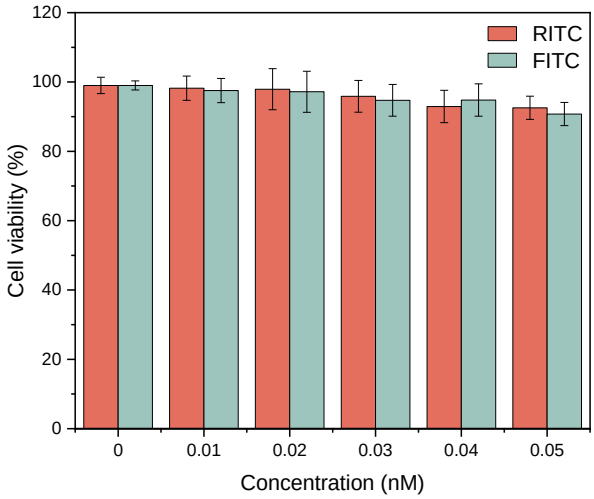

Figure 8. Cell viability assay. Cytotoxicity of the T cells was evaluated by cell counting kit-8 (CCK-8) assay after incubation with designed nanoprobes at different concentrations for 4 hours. Data was obtained from three independent samples. Measurements are presented as mean ± SD.

3.6 $CD8^+$ T Cell Activation

The $CD8^+$ T cells were activated using dynabeads mouse T-activator CD3/CD28 kit according to the manufacturer's protocol. Cell images were captured at various time points to track the progression of activation (Figure 9). Upon incubation with Dynabeads, which emulate in vivo T cell activation by antigen-presenting cells, aggregates formed between the beads and T cells. This process persisted from day 1 to day 5. By day 7, the morphology of T cells had transformed from small and spherical to elongated or flattened, signifying the differentiation of naïve T cells into activated T cells such as effector or memory T cells. Furthermore, there was a substantial

increase in cell numbers from 2,780,000 to 7,280,000 per mL over the course of days 0 to 7, indicating significant T-cell proliferation (Figure 10). These findings validate the successful activation of naïve T cells.

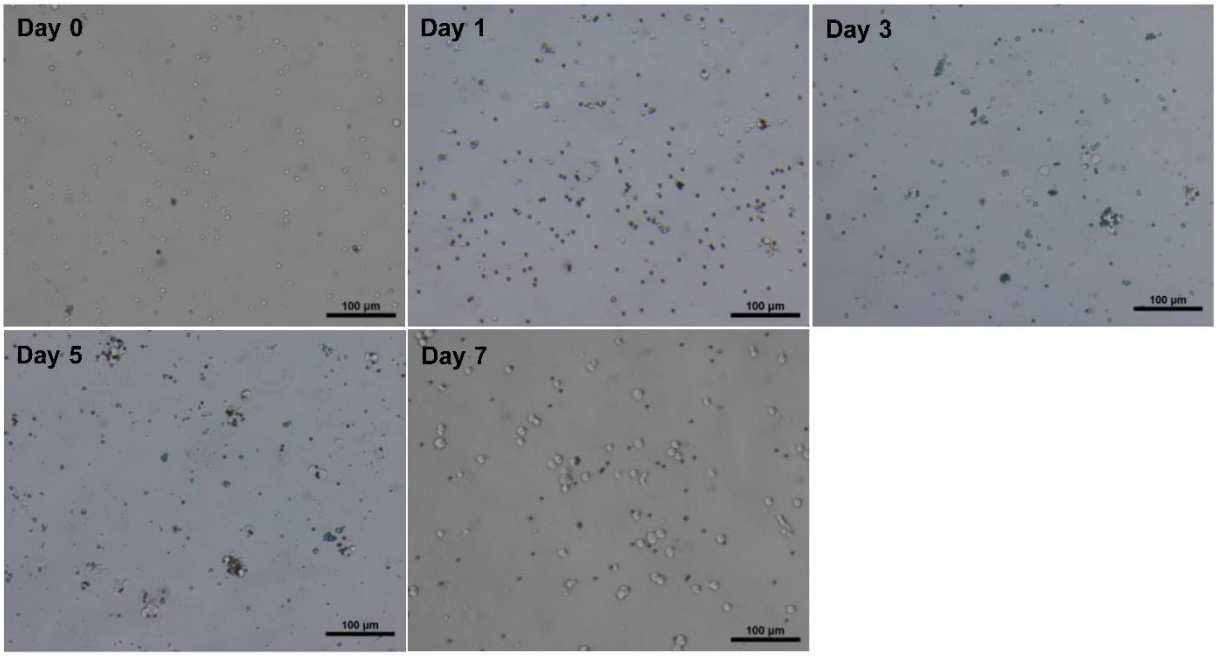

Figure 9. Cell images at different time points following activation.

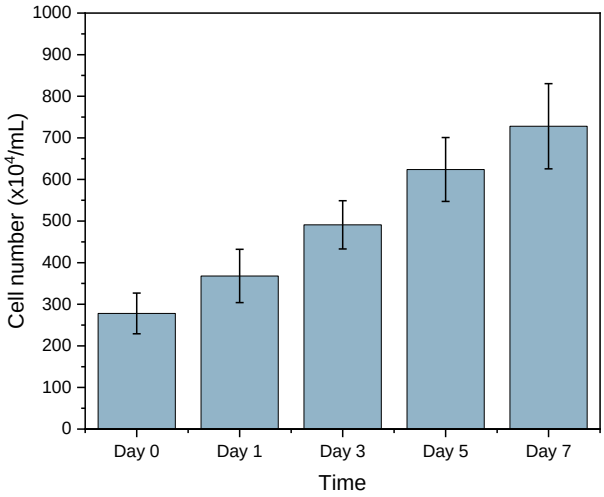

Figure 10. Cell quantification at different time points following activation. Data was obtained from three independent samples. Measurements are presented as mean ± SD.

3.7 Expression Changes of miRNA-21 and miRNA-150 during T Cell Differentiation

Numerous miRNA profiling studies demonstrated that there were major changes in the gene expression level of miRNA during different states of cytotoxic $CD8^+$ T cell, postulating that miRNA played a vital role in regulating $CD8^+$ T cell differentiation and controlled its survival and function[12, 13] Notably, miRNA-150 and miRNA-21 are prominently expressed and exhibit profound changes in gene expression among $CD8^+$ T cell subsets. Our qRT-PCR results in Figure 11 corroborate these findings, demonstrating that the relative expression level of miRNA-150 decreased from day 0 to day 5, while the relative expression level of miRNA-21 increased during this period. However, after seven days of activation, the relative expression level of miRNA-150 increases, while that of miRNA-21 declines slightly. The distinct and dynamic intracellular levels of miRNA-150 and miRNA-21 during T cell differentiation inspired us to investigate whether the intracellular tracking of miRNA-150 and miRNA-21 can assist in the monitoring of T cell differentiation or the identification of T cell subsets.

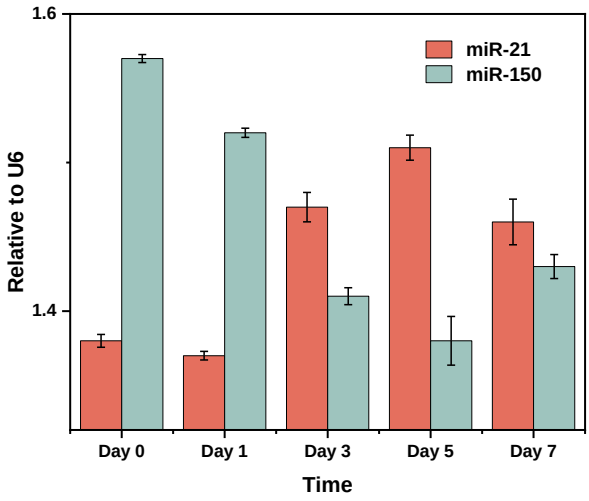

Figure 11. qRT-PCR result. The expression level of miR-21 and miR-150 was relative to U6 as an endogenous control. Data was expressed as mean ± SD (n=3).

3.8 Identification of T cell phenotypes from CD44/CD62L

To identify CD 8^+ T cell subtypes, flow cytometry was conducted to categorise different subsets based on the differential expression of surface biomarkers CD44 and CD62L. Extensive research has affirmed that CD8 T^+ cells can be classified into distinct phenotypes, including naïve, effector, and memory, based on their expression of CD62L and CD44. In this classification, the CD44-/CD62L+ population is designated as naïve T cell (T_N), the CD44+/CD62L+ population as central memory T cell (T_{CM}), and the CD44+/CD62L- population as effector T cell (T_E)[75-77]. The distribution of T cell phenotypes over time is depicted in Figure 12. Initially, on day 0, T cells were predominantly in a naïve state at 91.8%, while 5.8% were classified as central memory T cells. Following activation, the percentage of naïve T cells decreased to 42.8%, with effector and central memory T cells increasing to 4.26% and 41%, respectively, on day 1. Over subsequent days, the percentage of effector T cells peaked at 12.2% on day 5, subsequently decreasing to 7.82% on day 7. Concurrently, the percentage of naïve T cells continued to decline to a minimum of 4.76% on day 7, while central memory T cells progressively increased, reaching a peak of 84% on day 7. This suggests a successful activation of naïve T cells, leading to their differentiation into either effector or central memory T cells within the span of 7 days. Notably, the highest abundance of effector T cells was observed on day 5, while central memory T cells reached their zenith on day 7.

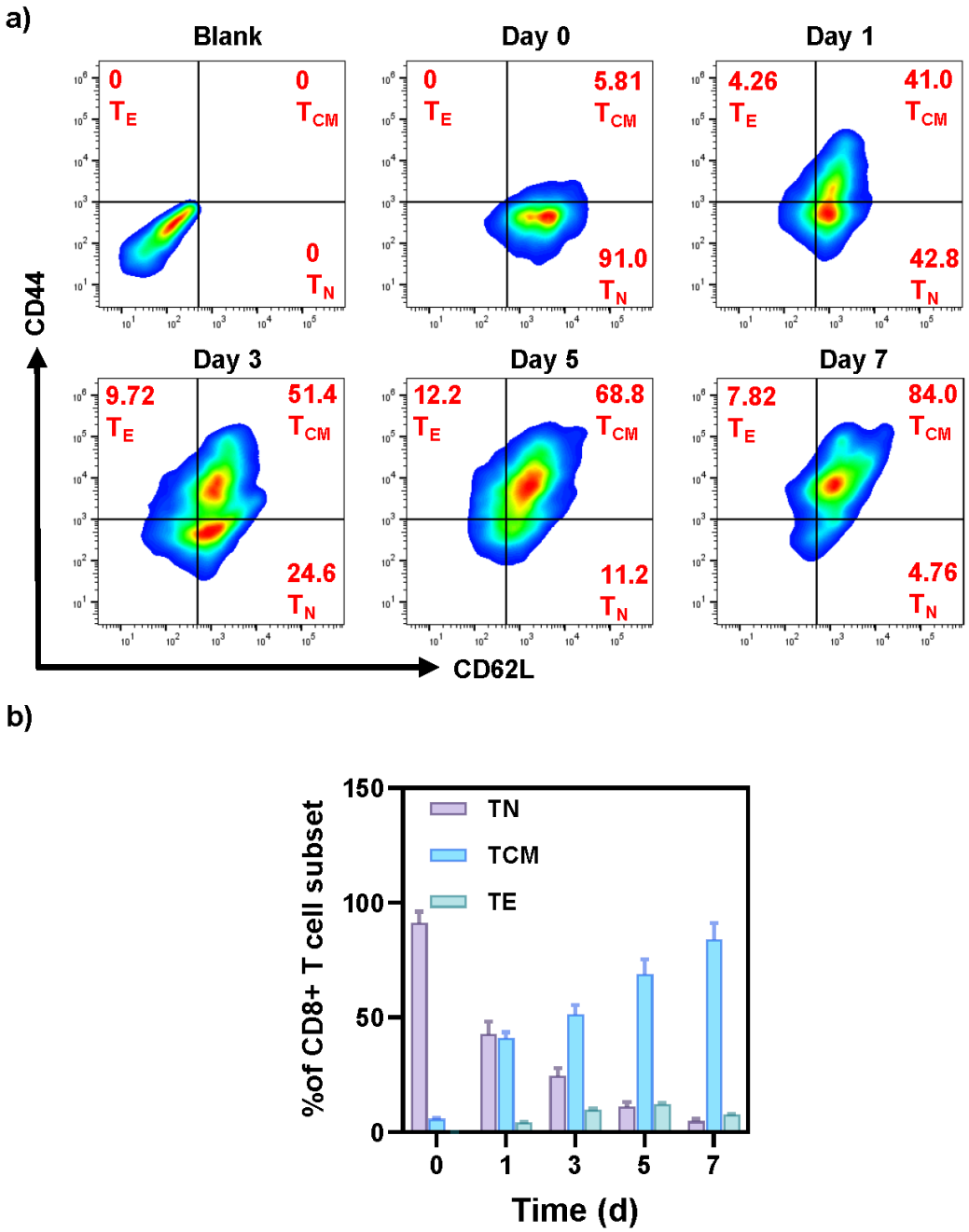

Figure 12. Identification of T cell subsets. (a) Flow cytometry quantification of the expression profile of surface activation markers (CD44/CD62L) on $CD8^+$ T cells before and after activation. The phenotypes are defined as the following: T_N, CD44-/CD62L+; T_E, CD44+/CD62L-; and T_{CM}, CD44+/CD62L+. (b) The relative proportion of the three T cell subsets on different time points of activation.

3.9 Identification of T cell phenotypes from miRNA-150/miRNA-21

To quantify the fluorescence intensity of the designed nanoprobes within CD8+ T cells, a flow cytometry analysis was conducted, and fluorescence signals were recorded across various activation days. The data illustrates the dynamic changes of miRNA-150 and miRNA-21 over the course of 7 days (Figure 13). The population of miRNA-150/miRNA-21 double-positive cells steadily increased from 16.7% on day 0 to 60.2% on day 7, suggesting an active involvement of miRNA-150 and miRNA-21 in the differentiation process (Figure 13a). Specifically, the expression level of miRNA-21 exhibited a notable increase from 1766 a.u. on day 0 to 4833 a.u. on day 7 (Figure 13b and 13c). In contrast, the expression level of miRNA-150 experienced a slight decrease from 3066 a.u. on day 0 to 2600 a.u. on day 3, followed by an increase to 2933 a.u. on day 7 (Figure 13b and 13c). In comparison between miRNA-150 and miRNA-21, the expression level of miRNA-150 was significantly higher than that of miRNA-21 on day 0, suggesting the presence of naïve T cells. On day 1 and day 3, the expression levels of miRNA-150 and miRNA-21 were comparable, implying the initiation of T cell differentiation is more favourable for central memory T cells, referring to Table 1. Moreover, on day 5 and day 7, the expression level of miRNA-21 surpassed that of miRNA-150, indicating an increasing number of effector and central memory T cells.

The results indicate a high expression of miRNA-150 and a low expression of miRNA-21, suggesting a substantial population of naïve T cells at the outset. As the study progresses, there is a notable increase in the number of effector and central memory T cells, particularly after day 1. However, it's worth noting that precisely identifying central memory T cells and effector T cells can be challenging. This is due to the limitations of flow cytometry, which provides an overall expression ratio of miRNA-150 and miRNA-21, offering limited insight into the specific phenotypes of individual T cells. Confocal images may be an alternative mean for a more detailed characterisation of T cell subtypes.

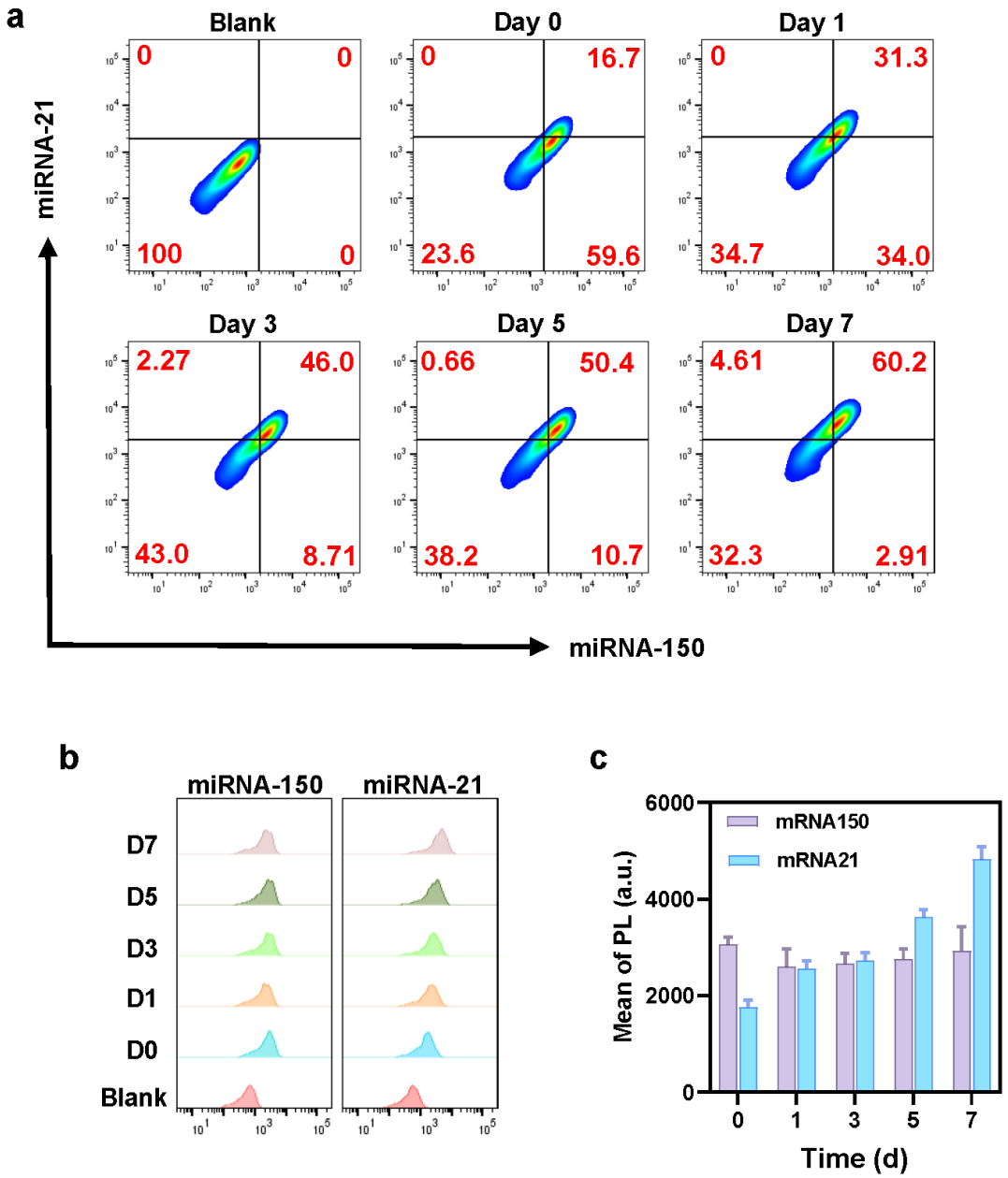

Figure 13. Flow cytometry analysis. (a) Dotted plots of FITC-coated and RITC-coated $AuSiO_2$ nanoprobes fluorescent signals by flow cytometry in the $CD8^+$ T cell under various activation days. (b) Histogram quantification of miRNA-150 and miRNA-21 channel. Incubation time: 4 h (c) Mean of the photoluminescence intensity of miRNA-150 and miRNA-21 channel.

3.10 Intracellular Imaging and miRNA Sensing

To determine the optimal incubation time for confocal imaging, 0.05 nM of nanoprobes that specifically recognised miRNA-150 and miRNA-21 were incubated with activated $CD8^+$ T cells. Subsequently, $CD8^+$ T cells were thoroughly rinsed with a cell growth medium. Confocal images were acquired at different time points, including 0.5, 2, 4 and 6 hours after the introduction of the nanoprobe (Figure 14). Representative confocal images revealed a gradual increase in fluorescence intensity for both miRNA-150 (green channel) and miRNA-21 (red channel) during the first 4 hours, indicating an ongoing cellular uptake of the designed nanoprobe. Quantitative analysis of fluorescence intensities, as shown in Figures 16a and 16b, further confirmed this increasing trend for both miRNA-150 and miRNA-21 within the first 4 hours, with a slight decline observed after a 6-hour incubation period. Consequently, the optimal incubation time selected for subsequent cellular studies was determined to be 4 hours.

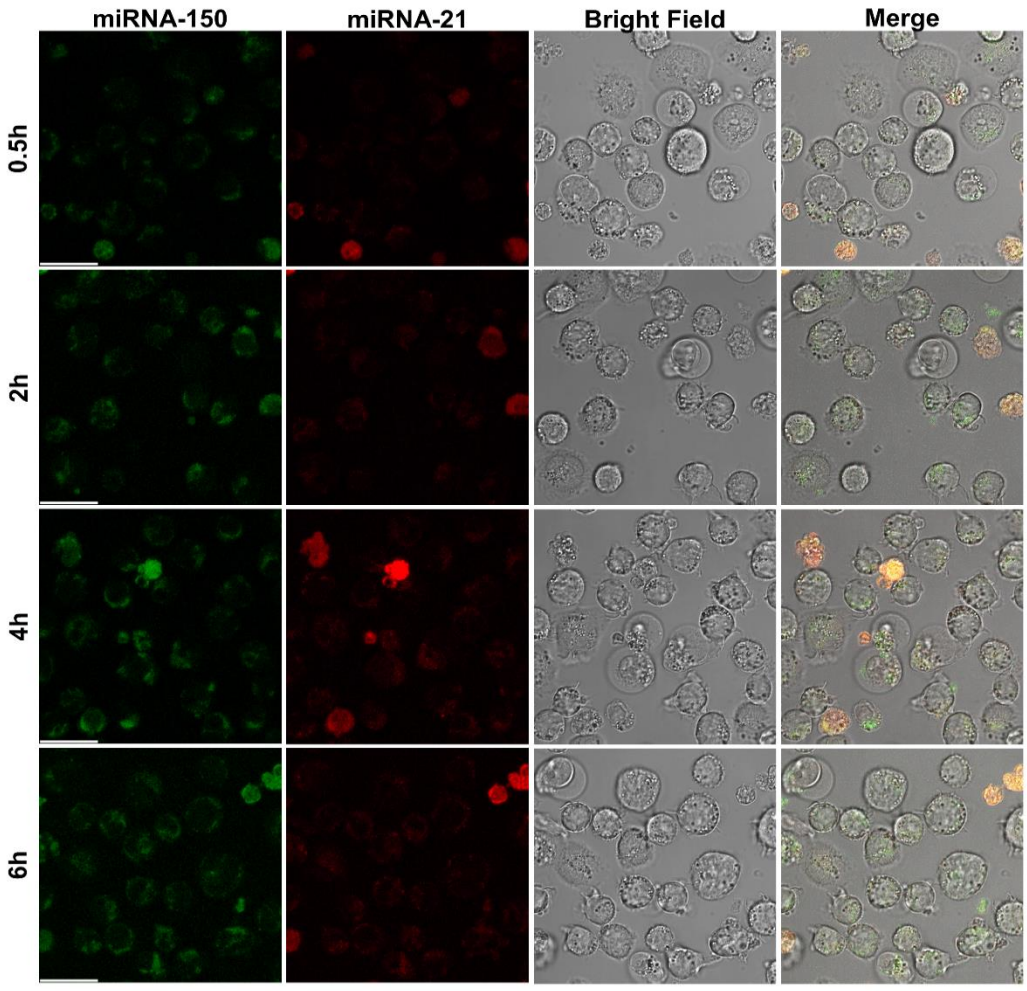

Figure 14. Confocal images of activated $CD8^+$ T cells on day 1 incubated with FITC-coated and RITC-coated $AuSiO_2$ nanoprobes at different time points. Scale bar: 20 um, miR-150 (FITC, Ex=488nm, Em=495-550nm), miR-21(RITC, Ex=560, Em=580-650nm)

To investigate the capability of multiplexed detection, 0.05 nM of nanoprobes were composed of 0.025nM of FITC-coated and 0.025nM RITC-coated $AuSiO_2$ nanoparticles with 140 ug/ml GO, which specifically recognised miRNA-150 and miRNA-21 respectively were incubated with naïve and activated $CD8^+$ T cell in cell growth medium (RPMI 1640 containing 10% FBS and 1% Pen/S) on day 0, day 1, day 3, day 5, and day 7 to investigate expression changes in cellular level of miRNA-150 and miRNA-21. Confocal images were taken after 4 hours of incubation. The naïve T cell on day 0 exhibited a higher fluorescence intensity of miRNA-150 (green channel) compared to miRNA-21 (red channel), as illustrated in Figure 15. The fluorescence intensities were quantified and presented in Figures 16c and 16d. These findings aligned with the high initial relative expression level of miRNA-150 and the low initial relative expression level of miRNA-21, as indicated by the qRT-PCR results in Figure 11 and literature[12]. This consistency suggests that the designed nanoprobes are proficient at detecting cellular miRNA at varying expression levels. Moreover, the substantial difference in fluorescence responses between the green and red channels on day 0 highlights the specificity and sensitivity of the designed nanoprobe in detecting cellular miRNA-150 and miRNA-21 in living naïve $CD8^+$ T cells. Furthermore, this demonstrates the nanoprobe's ability to simultaneously detect miRNA-150 and miRNA-21 in living naïve $CD8^+$ T cells, emphasising its capability for multiplexed detection.

In addition to the multiplexed detection, cellular expression level changes of miRNA-150 and miRNA-21 during T-cell differentiation were investigated. Representative confocal images depicted the dynamic changes in fluorescence intensity over a 7-day monitoring period (Figure 15). The fluorescence intensity of miRNA-21 (red channel) exhibited a significant increase over time from day 0 to day 7 and became intense on day 7 (Figure 15). Conversely, the fluorescence intensity of miRNA-150 (green channel) slightly decreased from day 0 to day 3 and then gradually increased from day 5 to day 7 (Figure 15). Importantly, the fluorescence intensity of miRNA-150 (green channel) was at its lowest on day 3 when compared to day 0 and day 5 (Figure 15). The aforementioned fluorescence intensities were quantified in Figures 16c and 16d. Furthermore, the bright-field images confirmed that the naïve $CD8^+$ T cells were viable in the imaging experiment, and the merged images showed a shift in colour from green on day 0 to orange on day 7. For instance, confocal images on day 7, three white arrows pointed to the T cells with higher expression levels of miRNA-21 (red channel) than miRNA-150 (green channel), indicating that these were potential effector T cells. This demonstrates that the

designed nanoprobe successfully captures changes in the concentrations of miRNA-150 and miRNA-21 during $CD8^+$ T cell differentiation. Moreover, it suggests the possibility of identifying distinct T cell subsets based on miRNA expression patterns.

Indeed, from a miRNA perspective, both qRT-PCR and flow cytometry data measure the overall expression levels of miRNA-150 and miRNA-21 at specific time points, which provide limited insight into the phenotypes of individual T cells. However, through confocal images, we can identify which cells have higher miRNA-150 or miRNA-21 content, allowing us to determine whether they are central memory T cells or effector T cells. Integrating the assessment of miRNA content in specific T cells with the identification of T cell phenotypes can offer novel insights into T cell therapy. The manipulation of miR-150 or miRNA-21 levels or activity presents a promising avenue in immunotherapeutic strategies aimed at augmenting T-cell responses against various diseases.

In summary, miRNA-150 and miRNA-21 emerge as pivotal regulatory components in the complex coordination of $CD8^+$ T cell behaviour, exerting influence over T cell differentiation, as well as effector and central memory T cell functions. This underscores their potential in therapeutic interventions. The tracking of miRNA expression during T-cell differentiation holds paramount scientific significance within the realm of immunology research. This investigation provides a unique window into the intricate regulatory mechanisms governing the fate determination of T cells. MiRNAs, known for their pivotal roles in post-transcriptional gene regulation, emerge as key players in orchestrating this differentiation process. By scrutinising the dynamic expression patterns of miRNAs, such as the notable miRNA-150 and miRNA-21 in this study, a deeper comprehension of the underlying molecular network governing T-cell behaviour is attained. This knowledge is integral not only for delineating the fundamental regulatory processes but also for paving the way towards targeted therapeutic interventions. The potential to manipulate miRNA levels or activity presents an exciting avenue for immunotherapeutic strategies, promising enhanced T-cell responses against a spectrum of diseases. Moreover, this investigation contributes to the burgeoning field of personalised medicine, where tailoring interventions based on individual miRNA profiles may lead to more effective and tailored treatments. Furthermore, the identification of specific miRNA signatures holds promise as valuable biomarkers for disease monitoring and treatment response assessment. In essence, this study not only advances our understanding of fundamental

immunology processes but also holds far-reaching implications for clinical applications and the broader landscape of biomedical research.

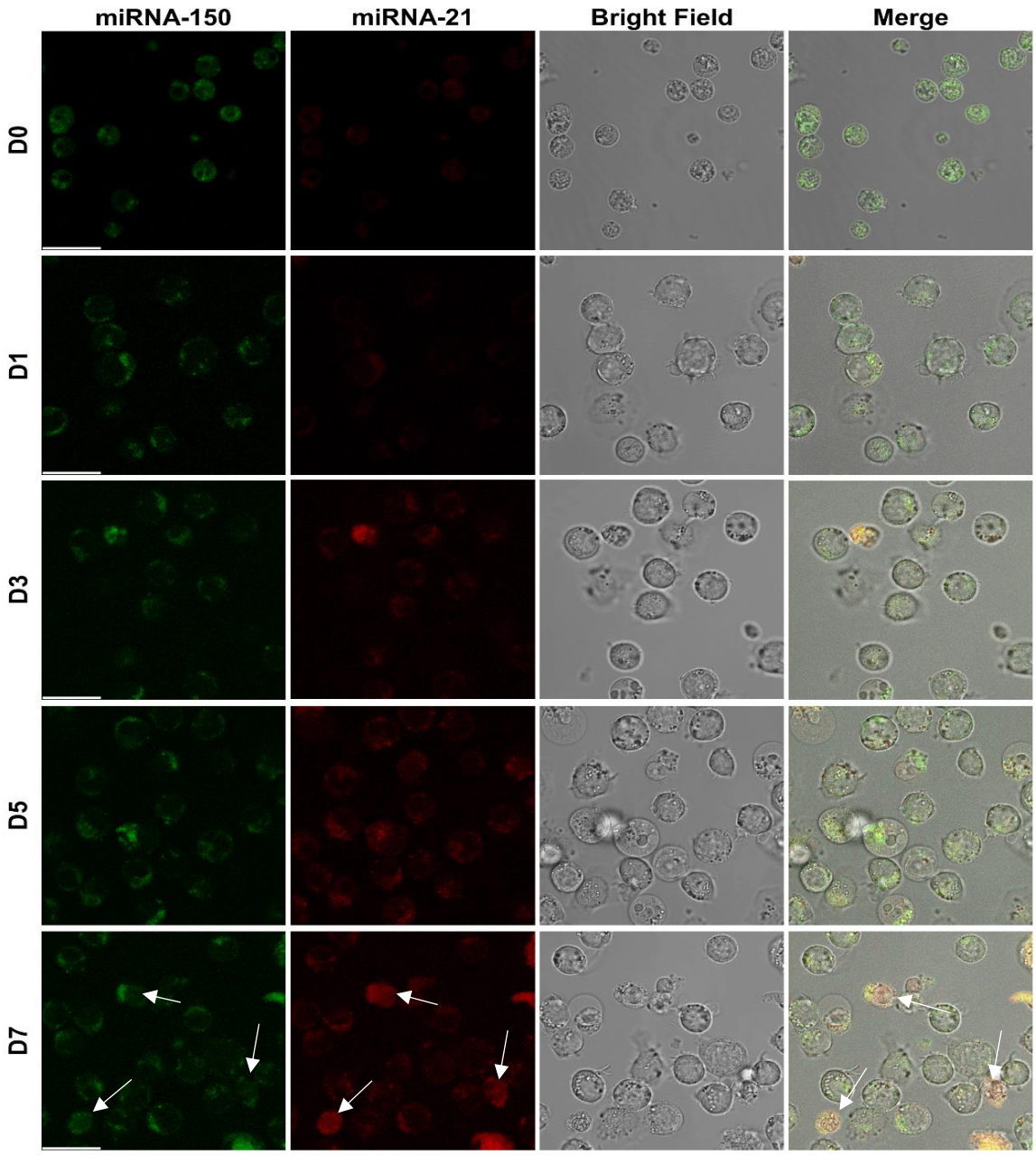

Figure 15. Confocal images of naïve on day 0 and activated $CD8^+$ T cells on day 1, 3,5 and 7 incubated with FITC-coated and RITC-coated AuSiO2 nanoprobes incubated for 4 hours. Scar bar: 20 um, miRAN-150 (Ex=488nm, Em=495-550nm), miRNA-21 (Ex=560, Em=580-650nm).

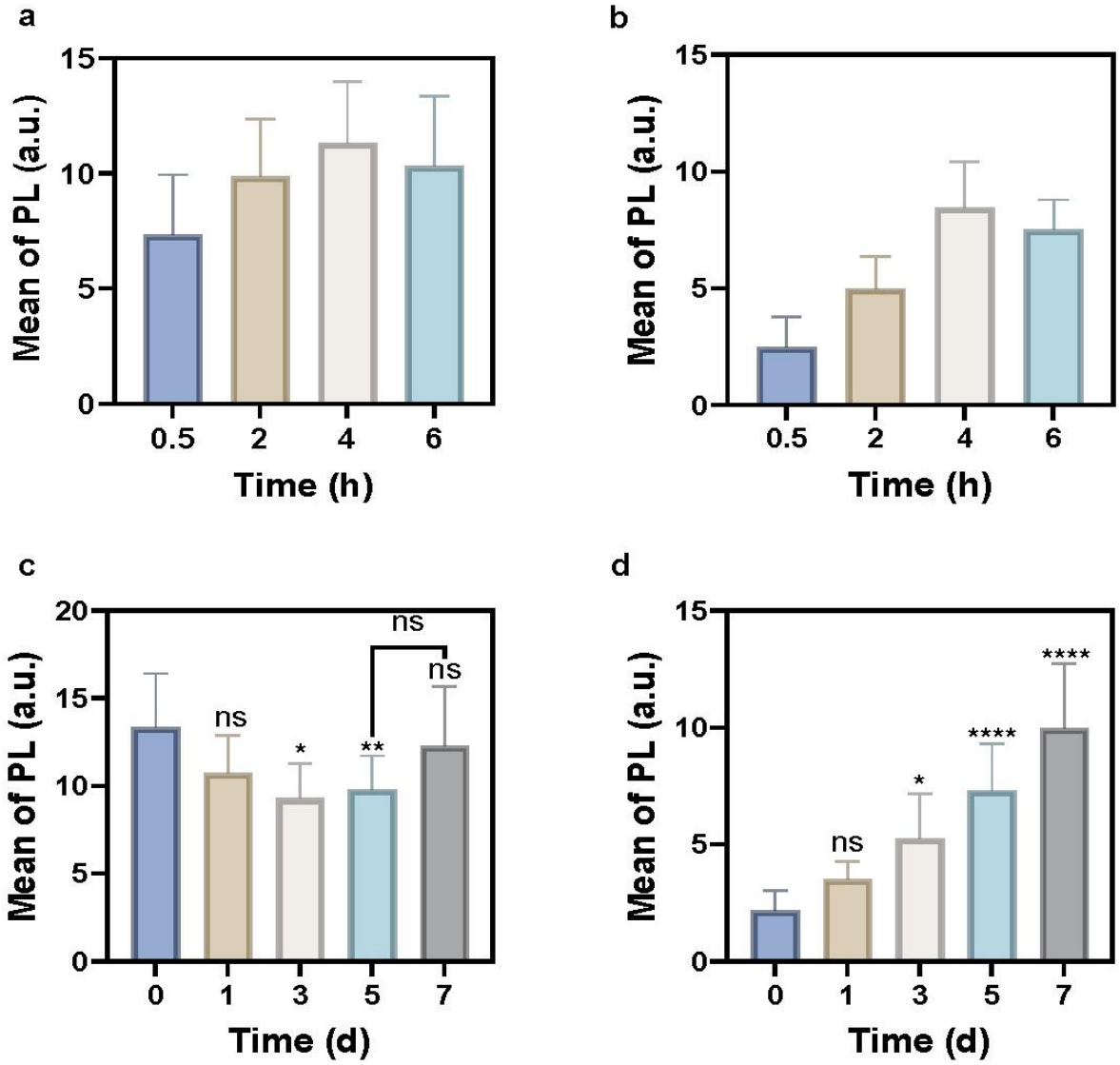

*Figure 16. Quantification of photoluminescence intensity of miRNA-150 channel (a) and miRNA-21 channel (b) at different incubation times. Quantification of photoluminescence intensity of (c) miRNA150 channel and (d) miRNA21 channel after 4 h incubation on day 0, day 1, day 3, day 5 and day 7. One-way ANOVA with Tukey's multiple comparisons. Fluorescence intensities were quantified and were expressed as mean ± SD. (ns: no significance,p< 0.05, **p< 0.005, *p< 0.0005, and ***p< 0.0001, n= 3, one-way ANOVA test).*

3.11 Summary

In this study, a metal-enhanced fluorescence nanoprobe was developed for exploring T-cell subtypes. The optimal metal-enhanced fluorescence effect was achieved when the silica shell thickness was 18 nm. The enhancement reached approximately 2.8 times higher for FITC and 1.8 times higher for RITC. The nanoprobes exhibited a linear response to target DNA concentration, with limits of detection (LoD) of 28.859 pM for FITC-coated $AuSiO_2$ and 38.43 pM for RITC-coated $AuSiO_2$. It exhibited sensitive DNA detection capabilities without the need for amplification steps. The nanoprobe demonstrated high stability and compatibility with cellular systems. Intracellular imaging and detection of miRNA-150 and miRNA-21 in $CD8^+$ T cells revealed dynamic changes in their expression levels during T cell differentiation. The designed nanoprobes exhibited multiplexed detection capabilities, allowing simultaneous monitoring of miRNA-150 and miRNA-21 in living $CD8^+$ T cells. Additionally, they showcased sensitivity to changes in miRNA expression levels during T cell differentiation, hinting at their potential for identifying distinct T cell subsets based on miRNA profiles.

Chapter 4 Conclusion

4.1 Conclusions

In this study, we successfully developed a metal-enhanced fluorescence nucleic acid-based nanoprobe to explore T-cell subtypes. The optimal fabrication of silica-coating gold core nanoparticles and the optimal distance between the fluorophores and the gold nanoparticles have been determined. The introduction of a thin layer of thiol PEG onto the AuNP surface played a crucial role in preventing aggregation, thus facilitating subsequent modifications. This protective coating established stable Au-S bonds, safeguarding the AuNPs from aggregation. Following this, a silica shell was grown on the PEG-coated AuNPs via hydrolysis and condensation of tetraethyl orthosilicate (TEOS) in the presence of ammonia. The silica shell's thickness was controllable by adjusting the volume of TEOS added. TEM analysis confirmed the successful synthesis of silica shells with varying thicknesses, ranging from 11 nm to 45 nm. These nanoparticles provide different distances between fluorophores and the gold nanoparticles for optimisation of the MEF effect. The following dynamic zeta potential changes results demonstrated the stepwise progression of particle development during synthesis and confirmed the successful preparation of the $AuSiO_2$ nanoparticles. The optimal metal-enhanced fluorescence effect was achieved when the silica shell thickness was 18 nm. The enhancement reached approximately 2.8 times higher for FITC and 1.8 times higher for RITC.

Notably, a secondary layer of silica coating was applied to these particles to facilitate DNA modification and stability. The designed nanoprobe exhibited potential for ultrasensitive DNA detection without amplification steps and high stability in various buffers. The maximum quenching efficiency was attained at 97% for RITC-coated $AuSiO_2$ nanoparticles and 98% for FITC-coated $AuSiO_2$ nanoparticles with an optimal GO concentration of 140 μg/ml. The nanoprobes exhibited a linear response to target DNA concentration, with limits of detection (LoD) of 28.859 pM for FITC-coated AuSiO2 and 38.43 pM for RITC-coated AuSiO2. Stability tests indicated excellent performance of the designed nanoprobes in TE buffer and cell culture medium over a 14-day period, with slight declines observed after 21 days. The protective second silica shell played a crucial role in preserving fluorescence stability during long-term monitoring.

Cell viability assays demonstrated that the nanoprobes exhibited favourable cellular compatibility, with cellular viability exceeding 90% at concentrations ranging from 0.01 nM

to 0.05 nM. Activation of $CD8^+$ T cells was successfully achieved, resulting in significant proliferation and differentiation into effector and central memory T cells. The flow cytometry analysis reveals distinct phenotypic shifts, with the population of miRNA-150/miRNA-21 double-positive cells showing a notable increase over the 7-day period. This suggests an active involvement of these miRNAs in the differentiation process. The observed changes in fluorescence intensity during confocal imaging further support this, indicating ongoing cellular uptake of the designed nanoprobe. Intracellular imaging and detection of miRNA-150 and miRNA-21 in $CD8^+$ T cells revealed dynamic changes in their expression levels during T cell differentiation. The designed nanoprobes exhibited multiplexed detection capabilities, allowing simultaneous monitoring of miRNA-150 and miRNA-21 in living $CD8^+$ T cells. Additionally, they showcased sensitivity to changes in miRNA expression levels during T cell differentiation, hinting at their potential for identifying distinct T cell subsets based on miRNA profiles.

In conclusion, this study presents a robust and versatile platform for ultrasensitive DNA detection and intracellular monitoring of miRNA-150 and miRNA-21, providing valuable insights into the dynamic changes of miRNA expression during T-cell differentiation. The designed nanoprobes exhibit high stability, cellular compatibility, and multiplexed detection capabilities, laying the groundwork for future applications in cellular studies and clinical diagnostics.

Based on the newly developed sensing platform in this study, several investigations can be further carried out to improve the performance. The current nanoprobe demonstrates an enhancement factor of approximately 2 to 3 times, constrained by the size and morphology of the gold nanoparticles. It is hypothesised that larger nanoparticles, such as gold nanoparticles with 100nm diameter, may exhibit a more pronounced scattering peak, potentially leading to stronger enhancement effects. Nevertheless, an increase in the size of gold nanoparticles might impede their cellular uptake capacity. To strike a balance between cellular uptake and enhancement effects, one potential solution could involve exploring the use of gold nanorods, which may offer the prospect of achieving even greater enhancement effects.

Furthermore, there is potential for enhancing sensing performance by optimising dye loading efficiency. The challenge in loading fluorophores onto amine-functionalized $AuSiO_2$ nanoparticles lies in the competition with time, particularly because the dye is highly susceptible to hydrolysis in water. To address this, a proposed solution involves pre-reacting

the dye with APTEs in absolute ethanol for 24 hours prior to loading onto the $AuSiO_2$ nanoparticles. This approach offers the dual advantage of increasing dye loading capacity while preventing hydrolysis in the water environment.

References

1. Borgulya, P., Kishi, H., Muller, U., Kirberg, J. & von Boehmer, H. Development of the CD4 and CD8 lineage of T cells: instruction versus selection. *EMBO J* **10**, 913-918 (1991).
2. Raskov, H., Orhan, A., Christensen, J.P. & Gogenur, I. Cytotoxic CD8(+) T cells in cancer and cancer immunotherapy. *Br J Cancer* **124**, 359-367 (2021).
3. Wong, W.K., Yin, B., Rakhmatullina, A., Zhou, J. & Wong, S.H.D. Engineering advanced dynamic biomaterials to optimize adoptive T-cell immunotherapy. *Engineered Regeneration* **2**, 70-81 (2021).
4. Ban, Y.H. *et al.* miR-150-Mediated Foxo1 Regulation Programs CD8(+) T Cell Differentiation. *Cell Rep* **20**, 2598-2611 (2017).
5. Liu, J., Wu, C.P., Lu, B.F. & Jiang, J.T. Mechanism of T cell regulation by microRNAs. *Cancer Biol Med* **10**, 131-137 (2013).
6. Gagnon, J.D. & Ansel, K.M. MicroRNA regulation of CD8(+) T cell responses. *Noncoding RNA Investig* **3** (2019).
7. Anfossi, S., Fu, X., Nagvekar, R. & Calin, G.A. MicroRNAs, Regulatory Messengers Inside and Outside Cancer Cells. *Adv Exp Med Biol* **1056**, 87-108 (2018).
8. Lu, L.-F. & Liston, A. MicroRNA in the immune system, microRNA as an immune system. *Immunology* **127**, 291-298 (2009).
9. Nguyen, H.T. *et al.* MiR-21 in the Cancers of the Digestive System and Its Potential Role as a Diagnostic, Predictive, and Therapeutic Biomarker. *Biology (Basel)* **10** (2021).
10. Trifari, S. *et al.* MicroRNA-directed program of cytotoxic CD8+ T-cell differentiation. *Proc Natl Acad Sci U S A* **110**, 18608-18613 (2013).
11. Vasilescu, C. *et al.* MicroRNA Fingerprints Identify miR-150 as a Plasma Prognostic Marker in Patients with Sepsis. *PLoS ONE* **4**, e7405 (2009).
12. Wu, H. *et al.* miRNA profiling of naive, effector and memory CD8 T cells. *PLoS One* **2**, e1020 (2007).
13. Gutierrez-Vazquez, C. *et al.* miRNA profiling during antigen-dependent T cell activation: A role for miR-132-3p. *Sci Rep* **7**, 3508 (2017).
14. Smith, N.L., Wissink, E.M., Grimson, A. & Rudd, B.D. miR-150 Regulates Differentiation and Cytolytic Effector Function in CD8+ T cells. *Sci Rep* **5**, 16399 (2015).
15. Chen, Z. *et al.* miR-150 Regulates Memory CD8 T Cell Differentiation via c-Myb. *Cell Rep* **20**, 2584-2597 (2017).
16. King, B.C. *et al.* CD46 Activation Regulates miR-150-Mediated Control of GLUT1 Expression and Cytokine Secretion in Human CD4+ T Cells. *J Immunol* **196**, 1636-1645 (2016).

17. Zhang, Z., Zhang, C., Li, F., Zhang, B. & Zhang, Y. Regulation of Memory CD8+ T Cell Differentiation by MicroRNAs. *Cell Physiol Biochem* **47**, 2187-2198 (2018).
18. Jeker, L.T. & Bluestone, J.A. MicroRNA regulation of T-cell differentiation and function. *Immunol Rev* **253**, 65-81 (2013).
19. Tsai, C.Y., Allie, S.R., Zhang, W. & Usherwood, E.J. MicroRNA miR-155 affects antiviral effector and effector Memory CD8 T cell differentiation. *J Virol* **87**, 2348-2351 (2013).
20. Liang, Y., Pan, H.-F. & Ye, D.-Q. microRNAs function in CD8+ T cell biology. *Journal of Leukocyte Biology* **97**, 487-497 (2015).
21. Ando, Y. *et al.* Overexpression of microRNA-21 is associated with elevated pro-inflammatory cytokines in dominant-negative TGF-β receptor type II mouse. *Journal of autoimmunity* **41**, 111-119 (2013).
22. Garchow, B.G. *et al.* Silencing of microRNA-21 in vivo ameliorates autoimmune splenomegaly in lupus mice. *EMBO Molecular Medicine* **3**, 605-615 (2011).
23. Iliopoulos, D., Kavousanaki, M., Ioannou, M., Boumpas, D. & Verginis, P. The negative costimulatory molecule PD-1 modulates the balance between immunity and tolerance via miR-21. *Eur J Immunol* **41**, 1754-1763 (2011).
24. Stagakis, E. *et al.* Identification of novel microRNA signatures linked to human lupus disease activity and pathogenesis: miR-21 regulates aberrant T cell responses through regulation of PDCD4 expression. *Ann Rheum Dis* **70**, 1496-1506 (2011).
25. Kim, C. *et al.* Activation of miR-21-Regulated Pathways in Immune Aging Selects against Signatures Characteristic of Memory T Cells. *Cell Rep* **25**, 2148-2162 e2145 (2018).
26. Kaech, S.M. & Cui, W. Transcriptional control of effector and memory CD8+ T cell differentiation. *Nat Rev Immunol* **12**, 749-761 (2012).
27. Kaech, S.M., Hemby, S., Kersh, E. & Ahmed, R. Molecular and functional profiling of memory CD8 T cell differentiation. *Cell* **111**, 837-851 (2002).
28. Nakajima, Y., Chamoto, K., Oura, T. & Honjo, T. Critical role of the CD44 ^{low} CD62L ^{low} CD8 ⁺ T cell subset in restoring antitumor immunity in aged mice. *Proceedings of the National Academy of Sciences* **118**, e2103730118 (2021).
29. Ye, J., Xu, M., Tian, X., Cai, S. & Zeng, S. Research advances in the detection of miRNA. *Journal of pharmaceutical analysis* **9**, 217-226 (2019).
30. Várallyay, E., Burgyán, J. & Havelda, Z. MicroRNA detection by northern blotting using locked nucleic acid probes. *Nature protocols* **3**, 190-196 (2008).

31. Li, W. & Ruan, K. MicroRNA detection by microarray. *Analytical and bioanalytical chemistry* **394**, 1117-1124 (2009).
32. Kang, K., Peng, X., Luo, J. & Gou, D. Identification of circulating miRNA biomarkers based on global quantitative real-time PCR profiling. *Journal of animal science and biotechnology* **3**, 1-9 (2012).
33. Dreaden, E.C., Alkilany, A.M., Huang, X., Murphy, C.J. & El-Sayed, M.A. The golden age: gold nanoparticles for biomedicine. *Chemical Society Reviews* **41**, 2740-2779 (2012).
34. Holzinger, M., Le Goff, A. & Cosnier, S. Nanomaterials for biosensing applications: a review. *Frontiers in chemistry* **2**, 63 (2014).
35. Le Ba, T., Mahian, O., Wongwises, S. & Szilágyi, I.M. Review on the recent progress in the preparation and stability of graphene-based nanofluids. *Journal of Thermal Analysis and Calorimetry* **142**, 1145-1172 (2020).
36. Gosai, A., Khondakar, K.R., Ma, X. & Ali, M.A. Application of functionalized graphene oxide based biosensors for health monitoring: Simple graphene derivatives to 3D printed platforms. *Biosensors* **11**, 384 (2021).
37. Sharma, D., Kanchi, S., Sabela, M.I. & Bisetty, K. Insight into the biosensing of graphene oxide: Present and future prospects. *Arabian Journal of Chemistry* **9**, 238-261 (2016).
38. Liao, C., Li, Y. & Tjong, S.C. Graphene nanomaterials: Synthesis, biocompatibility, and cytotoxicity. *International journal of molecular sciences* **19**, 3564 (2018).
39. Wang, K. *et al.* Biocompatibility of graphene oxide. *Nanoscale Res Lett* **6**, 1-8 (2011).
40. Liu, J., Cui, L. & Losic, D. Graphene and graphene oxide as new nanocarriers for drug delivery applications. *Acta biomaterialia* **9**, 9243-9257 (2013).
41. Oliveira, A.M. *et al.* Graphene oxide thin films with drug delivery function. *Nanomaterials* **12**, 1149 (2022).
42. Kim, J., Cote, L.J., Kim, F. & Huang, J. Visualizing Graphene Based Sheets by Fluorescence Quenching Microscopy. *Journal of the American Chemical Society* **132**, 260-267 (2010).
43. Mei, Q. *et al.* Graphene oxide: from tunable structures to diverse luminescence behaviors. *Advanced science* **6**, 1900855 (2019).
44. Méndez-Romero, U.A., Velasco-Soto, M.A., Licea-Jiménez, L., González-Hernández, J. & Pérez-García, S.A. Long-term evolution of the chemical and structural stability of graphene oxide after storage as solid and as aqueous dispersion. *Nano Select* **2**, 2168-2175 (2021).

45. Campbell, E. *et al.* Graphene oxide as a multifunctional platform for intracellular delivery, imaging, and cancer sensing. *Scientific reports* **9**, 416 (2019).
46. Alex, S. & Tiwari, A. Functionalized gold nanoparticles: synthesis, properties and applications—a review. *Journal of nanoscience and nanotechnology* **15**, 1869-1894 (2015).
47. Carnovale, C., Bryant, G., Shukla, R. & Bansal, V. Identifying trends in gold nanoparticle toxicity and uptake: size, shape, capping ligand, and biological corona. *ACS omega* **4**, 242-256 (2019).
48. Kus-Liśkiewicz, M., Fickers, P. & Ben Tahar, I. Biocompatibility and cytotoxicity of gold nanoparticles: recent advances in methodologies and regulations. *International journal of molecular sciences* **22**, 10952 (2021).
49. Amendola, V., Pilot, R., Frasconi, M., Maragò, O.M. & Iatì, M.A. Surface plasmon resonance in gold nanoparticles: a review. *Journal of Physics: Condensed Matter* **29**, 203002 (2017).
50. Ayala-Orozco, C. *et al.* Fluorescence enhancement of molecules inside a gold nanomatryoshka. *Nano Lett* **14**, 2926-2933 (2014).
51. Bauch, M., Toma, K., Toma, M., Zhang, Q. & Dostalek, J. Plasmon-Enhanced Fluorescence Biosensors: a Review. *Plasmonics* **9**, 781-799 (2014).
52. Mayer, K.M. & Hafner, J.H. Localized surface plasmon resonance sensors. *Chem Rev* **111**, 3828-3857 (2011).
53. Amina, S.J. & Guo, B. A review on the synthesis and functionalization of gold nanoparticles as a drug delivery vehicle. *International journal of nanomedicine*, 9823-9857 (2020).
54. Tan, L.H., Xing, H., Chen, H. & Lu, Y. Facile and efficient preparation of anisotropic DNA-functionalized gold nanoparticles and their regioselective assembly. *Journal of the American Chemical Society* **135**, 17675-17678 (2013).
55. ChrisáLe, X. CRISPR/Cas12a-mediated gold nanoparticle aggregation for colorimetric detection of SARS-CoV-2. *Chemical Communications* **57**, 6871-6874 (2021).
56. Duan, H. *et al.* A CRISPR-Cas12a powered electrochemical sensor based on gold nanoparticles and MXene composite for enhanced nucleic acid detection. *Sensors and Actuators B: Chemical* **380**, 133342 (2023).
57. Lou, U.K., Wong, C.H. & Chen, Y. A simple and rapid colorimetric detection of serum lncRNA biomarkers for diagnosis of pancreatic cancer. *RSC advances* **10**, 8087-8092 (2020).
58. Ruang-Areerate, T. *et al.* Development of loop-mediated isothermal amplification (LAMP) assay using SYBR safe and gold-nanoparticle probe for detection of Leishmania in HIV patients. *Scientific reports* **11**, 12152 (2021).

59. Badshah, M.A. *et al.* Recent Developments in Plasmonic Nanostructures for Metal Enhanced Fluorescence-Based Biosensing. *Nanomaterials* **10**, 1749 (2020).
60. Ming, T., Chen, H., Jiang, R., Li, Q. & Wang, J. Plasmon-Controlled Fluorescence: Beyond the Intensity Enhancement. *The Journal of Physical Chemistry Letters* **3**, 191-202 (2012).
61. Hong, Y., Huh, Y.-M., Yoon, D.S. & Yang, J. Nanobiosensors Based on Localized Surface Plasmon Resonance for Biomarker Detection. *Journal of Nanomaterials* **2012**, 759830 (2012).
62. Kang, K.A., Wang, J., Jasinski, J.B. & Achilefu, S. Fluorescence manipulation by gold nanoparticles: from complete quenching to extensive enhancement. *J Nanobiotechnology* **9**, 16 (2011).
63. Peiris, S., McMurtrie, J. & Zhu, H.-Y. Metal nanoparticle photocatalysts: emerging processes for green organic synthesis. *Catalysis Science & Technology* **6**, 320-338 (2016).
64. Tserkezis, C., Stefanou, N., Wubs, M. & Mortensen, N.A. Molecular fluorescence enhancement in plasmonic environments: exploring the role of nonlocal effects. *Nanoscale* **8**, 17532-17541 (2016).
65. Jennings, T.L., Singh, M.P. & Strouse, G.F. Fluorescent Lifetime Quenching near d = 1.5 nm Gold Nanoparticles: Probing NSET Validity. *Journal of the American Chemical Society* **128**, 5462-5467 (2006).
66. Choi, J.H., Lim, J., Shin, M., Paek, S.H. & Choi, J.W. CRISPR-Cas12a-Based Nucleic Acid Amplification-Free DNA Biosensor via Au Nanoparticle-Assisted Metal-Enhanced Fluorescence and Colorimetric Analysis. *Nano Lett* **21**, 693-699 (2021).
67. Bastus, N.G., Comenge, J. & Puntes, V. Kinetically controlled seeded growth synthesis of citrate-stabilized gold nanoparticles of up to 200 nm: size focusing versus Ostwald ripening. *Langmuir* **27**, 11098-11105 (2011).
68. Fernández-López, C. *et al.* Highly Controlled Silica Coating of PEG-Capped Metal Nanoparticles and Preparation of SERS-Encoded Particles. *Langmuir* **25**, 13894-13899 (2009).
69. Häkkinen, H. The gold–sulfur interface at the nanoscale. *Nature chemistry* **4**, 443-455 (2012).
70. Liu, S. & Han, M. Synthesis, functionalization, and bioconjugation of monodisperse, Silica-Coated gold nanoparticles: Robust bioprobes. *Advanced Functional Materials* **15**, 961-967 (2005).
71. Cheng, D. & Xu, Q.-H. Separation distance dependent fluorescence enhancement of fluorescein isothiocyanate by silver nanoparticles. *Chemical communications*, 248-250 (2007).

72. Haiss, W., Thanh, N.T., Aveyard, J. & Fernig, D.G. Determination of size and concentration of gold nanoparticles from UV− Vis spectra. *Analytical chemistry* **79**, 4215-4221 (2007).
73. Ho, V. *et al.* Single cell quantification of microRNA from small numbers of non-invasively sampled primary human cells. *Communications Biology* **6**, 458 (2023).
74. Calvo-Lozano, O. *et al.* One-step and real-time detection of microRNA-21 in human samples for lung cancer biosensing diagnosis. *Analytical chemistry* **94**, 14659-14665 (2022).
75. Sckisel, G.D. *et al.* Differential phenotypes of memory CD4 and CD8 T cells in the spleen and peripheral tissues following immunostimulatory therapy. *Journal for ImmunoTherapy of Cancer* **5** (2017).
76. Samji, T. & Khanna, K.M. Understanding memory CD8 + T cells. *Immunology Letters* **185**, 32-39 (2017).
77. Weatherly, K. *et al.* Functional profile of S100A4-deficient T cells. *Immunity, Inflammation and Disease* **3**, 431-444 (2015).